Applied Catalysis B: Environment and Energy 364 (2025) 124839

Contents lists available at ScienceDirect

Applied Catalysis B: Environment and Energy

journal homepage: www.elsevier.com/locate/apcatb

Manipulating adsorbed hydrogen on lanthanum-modified CuO_x: Industrial-current-density CO_2 electroreduction to C_{2+} products or CH_4

Zeyu Guo [a], Huiwen Zhu [a,b], Zijun Yan [a], Lei Lei [c], Degao Wang [c], Ziyun Xi [a], Yirui Lian [a], Jiahui Yu [a], Kam Loon Fow [a], Hainam Do [a], Jonathan D. Hirst [d], Tao Wu [a], Mengxia Xu [a,*]

[a] Department of Chemical and Environmental Engineering, and New Materials Institute, University of Nottingham Ningbo China, Ningbo 315100, China
[b] College of Digital Technology and Engineering, Ningbo University of Finance & Economics, Ningbo 315175, China
[c] Engineering Laboratory of Advanced Energy Materials, Ningbo Institute of Materials Technology and Engineering Chinese Academy of Sciences, Ningbo 315201, China
[d] School of Chemistry, University of Nottingham, University Park, Nottingham NG7 2RD, UK

ARTICLE INFO

Keywords:
Electrochemical CO_2 reduction
H_2O dissociation
Kinetic isotopic effect
in situ spectroscopy
Density functional theory

ABSTRACT

The selective electrochemical CO_2 reduction reaction (CO_2RR) yields valuable C_{2+} and C_1 products, yet the influence of adsorbed hydrogen (*H) on product distribution remains inadequately understood. This study explores this effect by developing bimetallic copper-based electrocatalysts with varied lanthanum (La) doping ratios. The oxide-derived (OD)-$La_{0.10}$-CuO_x catalyst exhibits a Faradaic efficiency (FE) over 80% for C_{2+} products at 300 mA cm^{-2}, whereas OD-$La_{0.40}$-CuO_x achieves a 61.4% FE_{CH4} at 400 mA cm^{-2}. Kinetic isotope experiments reveal distinct dependencies of the rate-determining steps on *H transfer for CO_2RR in OD-$La_{0.10}$-CuO_x and OD-$La_{0.40}$-CuO_x. *In situ* ATR-SEIRAS and DFT calculations demonstrate that the moderate H_2O dissociation capability of OD-$La_{0.10}$-CuO_x lowers the energy barrier for *CHO → *OCCHO conversion, thus increasing the FE_{C2+}. Conversely, OD-$La_{0.40}$-CuO_x, with its strong H_2O dissociation capability, favors *CHO → *CH_2O, thereby promoting CO_2RR-to-CH_4. These findings advance the understanding of the role of *H in CO_2 electroreduction at industrial current densities and present avenues for tailored CO_2RR products via doping engineering.

1. Introduction

The direct electrochemical carbon dioxide reduction reaction (CO_2RR), driven by renewable energy, represents a promising approach for achieving sustainable carbon-neutral energy conversion [1,2]. This environmentally friendly strategy enables carbon recovery while simultaneously producing valuable chemicals and fuels [3,4]. Among the various catalysts explored for CO_2RR, copper (Cu)-based catalysts facilitate CO_2 electroreduction toward multicarbon products at industrially relevant current densities (>200 mA cm^{-2}) [5]. This capacity is attributed to copper's negative adsorption energy for adsorbed CO (*CO) and positive adsorption energy for adsorbed hydrogen (*H), enabling complex coupling processes involving multiple proton and electron transfers [6]. CO_2RR products such as methane (CH_4), a 6-electron product, and ethylene (C_2H_4), a 12-electron product, are commonly used as high energy density fuels or high value-added chemicals [7–13]. Despite extensive research on high-performance Cu-based electrocatalysts, the structure-function relationships in CO_2RR and the reaction pathways to various products at industrial current densities are not fully understood. A better understanding of correlations among various products would offer the prospect of increasing the conversion efficiency of desired CO_2RR products.

In CO_2RR, multiple proton and electron transfer steps occur on the electrocatalyst surface, either sequentially or concurrently, leading to uncontrollable product distributions [14,15]. Researchers have elucidated CO_2RR selectivity using theoretical and experimental approaches. For the C_1 product formation, Liu et al. demonstrated that the rate-determining step (RDS) in the CO_2RR-to-CO pathway is the coupling of *CO_2^- with H^+ to form *COOH [16]. Xiong et al. revealed that the hydrogenation of *CO to *CHO is the RDS in the CO_2RR-to-CH_4 pathway, observing the *CHO intermediate using *in situ* Fourier transform infrared spectroscopy (FTIR) [17]. Toward C_{2+} hydrocarbon formation, C-C coupling is widely recognized as a crucial step. Kim and collaborators observed the formation of *OCCO species through C-C coupling during the CO_2RR-to-C_2 process at a Cu electrode, using *in situ* attenuated total reflectance–surface-enhanced infrared absorption spectroscopy (ATR-SEIRAS) [18,19]. An increased local *CO concentration facilitates further protonation of *CO-*CO coupling, progressing

* Corresponding author.
E-mail address: Mengxia.Xu@nottingham.edu.cn (M. Xu).

https://doi.org/10.1016/j.apcatb.2024.124839
Received 3 September 2024; Received in revised form 31 October 2024; Accepted 17 November 2024
Available online 19 November 2024

to *CHO-*CO coupling [20]. These studies highlight that proton/*H activation and transfer are integral to various CO_2RR pathways, particularly for synthesizing desirable hydrocarbons such as CH_4, C_2H_4, and other C_{2+} products.

Typically, protons involved in CO_2RR are derived from sources such as H_2O, H_3O^+ and HCO_3^- [21]. An isotope tracing study has demonstrated the direct role of H_2O in the electrochemical reduction of CO to ethanol [22]. Moreover, it is reported that accelerated H_2O dissociation kinetics can lower the energy barrier for formate formation [23]. Therefore, customizing H_2O dissociation to modulate local *H donors emerges as a promising strategy to facilitate CO_2RR, enabling tailored distributions of C_1 and C_{2+} products. The introduction of single-atom [24,25], oxygen vacancies [23], and rare-earth element doping, such as lanthanide [26], on catalyst surfaces has been reported to provide sites for H_2O dissociation. These sites expedite H_2O dissociation into *H, which subsequently participates in forming various hydrocarbons at CO_2 conversion sites [21,22,27]. Consequently, hydrocarbon production strongly depends on H_2O dissociation. Among these strategies for modulating *H, heteroatom doping can alter the charge density around active sites and affect reaction intermediates, thereby improving the activity and selectivity of Cu-based catalysts for CO_2RR [28]. Compared to d-block metal elements, the unique physical and chemical properties of lanthanides stem from the special positioning of their 4 f electrons and partially filled 5d orbitals. Specifically, lanthanum exhibits a high reduction potential (La^{3+}/La^0, −2.90 V vs RHE), remains stable during the CO_2RR process, and thus serves to modify the electronic structure of the Cu substrate [29]. For instance, La has been incorporated into constructs like $La(OH)_3$/Cu, Cu-based perovskite oxides, and Cu-based alloys for CO_2 electroreduction to various products [7,29,30].

While previous research has focused primarily on *H's effect on single product formation through CO_2RR, there is limited research on the branching pathways of CO_2RR to C_1 and C_{2+} products and their relationship with *H, particularly regarding *H transfer mechanisms in hydrogenation processes and competition with other intermediate formation processes such as dimerization. Although alkaline electrolytes commonly employed in industrial-current-density CO_2 electroreduction hinder H_2O dissociation and *H transfer, thus effectively inhibiting the hydrogen evolution reaction (HER), they also result in sluggish CO_2RR kinetics due to delayed *H activation and transfer [31,32]. Therefore, managing adsorbed hydrogen production and its transfer kinetics, and simultaneously suppressing HER is crucial for the rational design of high-performance CO_2RR electrocatalysts.

In this study, we synthesized a series of oxide-derived lanthanum-modified copper oxide (denoted as OD-La-CuO_x) catalysts with varied La doping to investigate the effect of *H on CO_2RR product distribution at industrial current densities. The results show that hydrocarbon selectivity shifts from C_{2+} products (in OD-$La_{0.10}$-CuO_x) to CH_4 (in OD-$La_{0.40}$-CuO_x) as La doping increases. Kinetic isotope effect (KIE) experiments and *in situ* electrochemical impedance spectroscopy (EIS) were employed to elucidate the role of *H transfer in forming various CO_2RR products. *In situ* ATR-SEIRAS and density functional theory (DFT) calculations reveal that La doping promotes H_2O adsorption and its dissociation to release *H. Additionally, the divergence between C_{2+} and CH_4 formation pathways lies in the subsequent conversion of *CHO. Specifically, during the CO_2RR-to-C_{2+} process, OD-$La_{0.10}$-CuO_x facilitates *CO protonation to *CHO and its further dimerization to *OCCHO, whereas OD-$La_{0.40}$-CuO_x promotes *CHO hydrogenation to *CH_2O, leading to CH_4 production.

2. Experimental section

2.1. Synthesis of La-CuO_x catalysts

The $La_{0.10}$-CuO_x catalyst was synthesized using a facile alcohol-thermal approach. Initially, $Cu(CH_3COO)_2{\cdot}H_2O$ (3 mmol, 0.6 g) and $La(NO_3)_3{\cdot}6H_2O$ (0.3 mmol, 0.13 g) were dissolved in 50 mL ethanol through sonication for 30 minutes with the lanthanum to copper molar ratio of 0.1–1. The resultant blue mixture was transferred into a Teflon-lined stainless-steel autoclave with a volume of 100 mL, and heated at 150 °C for 20 hours in an oven. After allowing the system to cool to room temperature naturally, the precipitates were washed three times with ethanol and deionized water before being dried at 70 °C overnight. Additionally, CuO_x was synthesized under identical conditions without the inclusion of $La(NO_3)_3{\cdot}6H_2O$. Various La-modified CuO_x catalysts ($La_{0.40}$- CuO_x, $La_{0.20}$-CuO_x, $La_{0.13}$-CuO_x, and $La_{0.06}$-CuO_x) were prepared using a similar procedure, with adjustments in La-Cu ratios such that 1.2 mmol, 0.6 mmol, 0.4 mmol, and 0.2 mmol of $La(NO_3)_3{\cdot}6H_2O$ were added, respectively. The as-prepared catalysts was transformed into OD-La-CuO_x through electroreduction.

2.2. Preparation of electrodes

A commercially available carbon paper (YLS-30T), utilized as a gas diffusion electrode (GDE), was precisely cut to dimensions of 2.0 cm × 15.0 cm and thoroughly rinsed with deionized water. A catalyst weighing 30 mg, such as CuO_x, $La_{0.06}$-CuO_x, $La_{0.10}$-CuO_x, $La_{0.13}$-CuO_x, $La_{0.20}$-CuO_x, or $La_{0.40}$-CuO_x, was dispersed in a mixture containing 20 μL of Nafion solution (5 wt%) and 3 mL of isopropanol, followed by sonication for over an hour. This prepared catalyst slurry was sprayed onto the cleaned GDE using a handheld airbrush, achieving a catalyst loading of approximately 1 mg cm^{-2}. After drying the cathode electrodes in a vacuum oven at 60 °C for 10 minutes, they were sectioned into seven squares, each measuring approximately 2.0 cm × 2.0 cm.

2.3. Electrochemical performance tests

The electrochemical performance tests were conducted in a gas-fed flow cell configurated with either an anion exchange membrane (AEM, Fumasep FAA-3-PK-130) or a cation exchange membrane (CEM, Nafion 117), depending on the electrolyte used (1 M KOH and 1 M KCl) to satisfy the industrial requirement. The electrolyzer comprised three chambers: the airflow chamber (1.0 cm × 1.0 cm), the cathode chamber with the working electrode (2.0 cm × 2.0 cm) and an Ag/AgCl reference electrode (saturated with 3 M KCl), and the anode chamber containing nickel foam (2.0 cm × 2.0 cm). The active area of the catholyte chamber was 1.0 cm^2. A high-purity CO_2 gas stream (99.99%) was passed through the gas chamber at a rate of 50 sccm, controlled by a mass flow meter. The cathode chamber was supplied with 10 mL min^{-1} of 1 M KOH (for alkaline condition, pH = 13.6) and 1 M KCl (for neutral condition, pH = 6.4) aqueous electrolytes via a peristaltic pump, while the anode chamber was fed with 10 mL min^{-1} 1 M KOH aqueous electrolyte using another peristaltic pump. The gas flow rate between the gas-fed flow cell and the GC (Agilent 8890B) inlet was verified by a soap film flow meter (Sensidyne Gilibrator-2).

All electrolysis experiments were conducted using an electrochemical workstation (CHI 660E) equipped with a current booster (CHI 680D). Potentials were converted to values relative to the reversible hydrogen electrode (RHE) with manual iR_u compensation, following the equation below:

$$E\ (vs.\ \text{RHE}) = E\ (vs.\ \text{Ag/AgCl}) + 0.0591 \times \text{pH} + 0.210 - iR_u \times 0.85$$

Cyclic voltammetry (CV) scans were performed prior to each CO_2RR experiment to pre-activate the electrocatalyst and remove organic residues present on the electrode surface, using 20 cycles over a potential range of −0.6 to −2.0 V relative to Ag/AgCl. Gas products (H_2, CO, CH_4 and C_2H_4) were monitored in real-time by connecting a GC inlet directly to the cathode chamber. The GC system is equipped with two flame ionization detectors (FID, the back FID for CO and CH_4; the front FID for C_2-C_3 hydrocarbons) and a thermal conductivity detector (TCD for H_2) for the identification and quantitative analysis of these products. Faradaic efficiencies of the gas products were determined using Eq. S1 from

the raw GC data. Liquid products were quantified using proton nuclear magnetic resonance (^{1}H NMR, Bruker DPX 400 MHz) with a water suppression technique. An internal standard was prepared by mixing 150 μL of dimethyl sulfoxide (DMSO) with 300 mL of ultrapure water. The NMR test solution consisted of 500 μL electrolyte, 100 μL D_2O, and 100 μL of aqueous DMSO (containing 0.05 μL DMSO) (Eq. S2 and Fig. S1). Cathodic energy efficiency was computed based on the CO_2RR at the cathode coupled with water oxidation reaction at the anode following Eq. S3. The Tafel slope for CO_2RR was calculated according to Eq. S4.

Additional details of the chemicals used, catalyst characterizations, product analysis, *in situ* ATR-SEIRAS measurements, and DFT computational methods are provided in the Supporting Information.

3. Results and discussion

3.1. Synthesis and characterizations

The lanthanum-modified CuO_x nanoparticles, synthesized with various La-doping molar ratios, were used as pre-electrocatalysts. As depicted in Fig. 1**a**, these catalysts were produced using a one-pot alcohol-thermal approach. The molar ratio of Cu to La was controlled by adjusting the concentration of the La precursor solution. Specifically, the La content for $La_{0.10}$- CuO_x and $La_{0.40}$- CuO_x was measured at 9.9 wt % and 25.6 wt%, respectively, by inductively coupled plasma mass spectrometry (ICP-MS) (Table S1). This facile synthesis method involves the decomposition of $Cu(CH_3COO)_2{\cdot}H_2O$ and $La(NO_3)_3{\cdot}6H_2O$ into mixed-phase metal oxide catalysts in the presence of ethanol. Under alcohol-thermal conditions within a Teflon-lined stainless-steel autoclave, an esterification reaction between acetate and ethanol readily occurs. Previous research has confirmed the formation of ethyl acetate in reaction solvents through gas chromatography (GC) with a flame ionization detector (FID) [33].

Transmission electron microscopy (TEM) was employed to examine the structural morphology of the as-prepared La-modified CuO_x electrocatalysts. The CuO_x nanoparticles, synthesized without La $(NO_3)_3{\cdot}6H_2O$, display regular particle sizes of under 10 nm (Fig. S2). As shown in Fig. 1**b and** S3, low-level La doping (i.e., $La_{0.10}$- CuO_x) has a minimal impact on morphology, maintaining an average particle size of roughly 6 nm. However, with increased La doping (i.e., $La_{0.40}$-CuO_x), the original particle morphology is not preserved. Fig. 1**c** and S4 show that ultra-small nanoparticles tend to agglomerate and increase in size. High-angle annular dark-field scanning transmission electron microscopy (HAADF-STEM) images and corresponding energy-dispersive X-ray spectroscopy (EDS) element maps reveal a uniform distribution of O, Cu, and La elements (Fig. 1**b** and **c,** Figs. S5 and S6) and indicate the integration of La into the fabricated material. Additionally, high-resolution TEM (HRTEM) was applied to reveal the lattice fringe characteristics of the synthesised La- CuO_x catalysts. The HRTEM images of both $La_{0.10}$- CuO_x and $La_{0.40}$- CuO_x exhibit abundant grain boundaries, with lattice edges in multiple orientations (Figs. S7 and S8). The grain boundaries of $La_{0.10}$-CuO_x are highlighted by white dotted lines in Fig. S7, resulting from the incorporation of heteroatoms into the material via doping. This introduction disrupts the ordered lattice structure and crystal growth, leading to defect formation and high-density grain boundaries within the material [26].

To verify the phase composition of the synthesized La-CuO_x catalysts, powder X-ray diffraction (PXRD) analyses were performed on both the

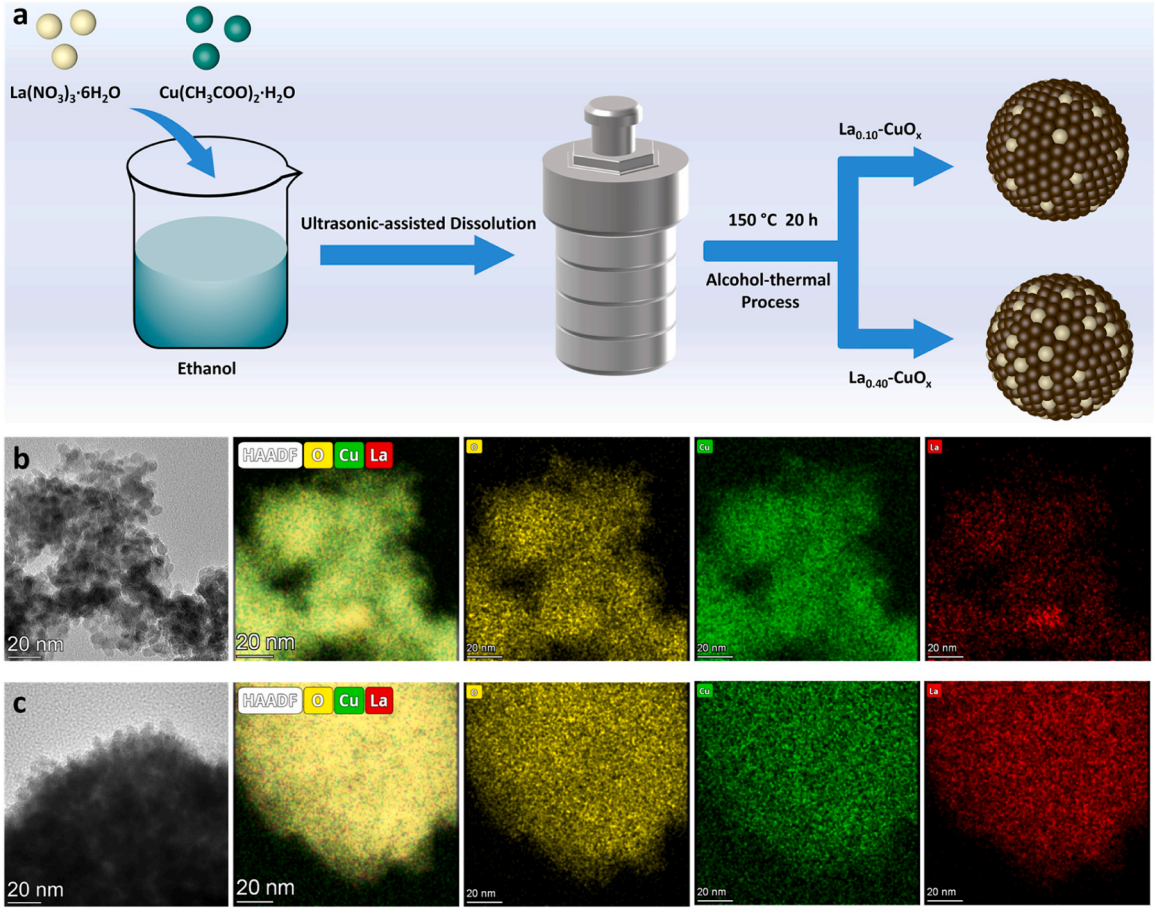

Fig. 1. a) Schematic illustration of the synthetic procedures of CuO_x and La-CuO_x catalysts. TEM image, HAADF-STEM image, and corresponding EDS element maps of b) $La_{0.10}$- CuO_x and c) $La_{0.40}$- CuO_x.

pure CuO_x and La-CuO_x catalysts (Fig. 2**a**). For CuO_x without La doping, the diffraction peaks can be precisely indexed to the monoclinic pure phase of CuO (JCPDS# 45–0937) with the most intense peaks at 35.6° for CuO (002) and 38.7° for CuO (111). When La is incorporated in small amounts, from $La_{0.06}$-CuO_x to $La_{0.10}$-CuO_x, the XRD patterns show a composition of CuO and Cu_2O (JCPDS# 05–0667). As La-doping increases, the diffraction peaks of CuO (002) and (111) weaken, while the peak for Cu_2O (111) becomes more pronounced. This behavior is attributed to the ability of trivalent La to modify the CuO electronic structure, initiating possible redox reactions [26], such as the replacement of Cu^{2+}-O^{2-}-Cu^{2+} pairs with Cu^{+}-O^{2-}-La^{3+} pairs to maintain electroneutrality [34]. With significant La doping, particularly from $La_{0.13}$-CuO_x to $La_{0.40}$-CuO_x, additional crystalline phase is observed, attributed to La_2CuO_4 (as per JCPDS# 30–0487), with increasing peak intensity. Concurrently, the diffraction peaks of CuO and Cu_2O diminish, with some eventually disappearing. Notably, the Cu_2O (111) and CuO ($\bar{1}13$) facet peaks of La-CuO_x with higher La doping levels are slightly shifted to lower diffraction regions compared to $La_{0.06}$-CuO_x and undoped CuO_x, respectively (Fig. S9). This shift is attributed to the doped La atoms, which have a larger atomic radius than Cu atoms [35, 36]. The Raman spectra of CuO_x show three peaks at 285, 336, and 619 cm^{-1} (Fig. S10), which correspond to the A_g, B_{g1} and B_{g2} vibration modes of CuO, respectively. The Raman peaks for $La_{0.10}$-CuO_x are shifted to higher wavenumbers, indicating changes in the electronic structure of CuO due to La doping. Moreover, a new Raman peak at 217 cm^{-1} is assigned to the $2\Gamma_{12}^{-}$ phonon modes of the Cu_2O [35,36].

Following CO_2RR at a current density of 300 mA cm^{-2} in 1 M KCl for 30 minutes, the OD-CuO_x only displays the characteristic peaks of the metallic Cu phase (Fig. S11a). In contrast, the OD-$La_{0.10}$-CuO_x retains peaks corresponding to the Cu_2O phase, dominated by the (111) facets, even after 60 minutes (Figs. 2**b**, S11b and S12). This is likely due to the construction of unconventional 4f-2d-3d hybrid orbitals through La

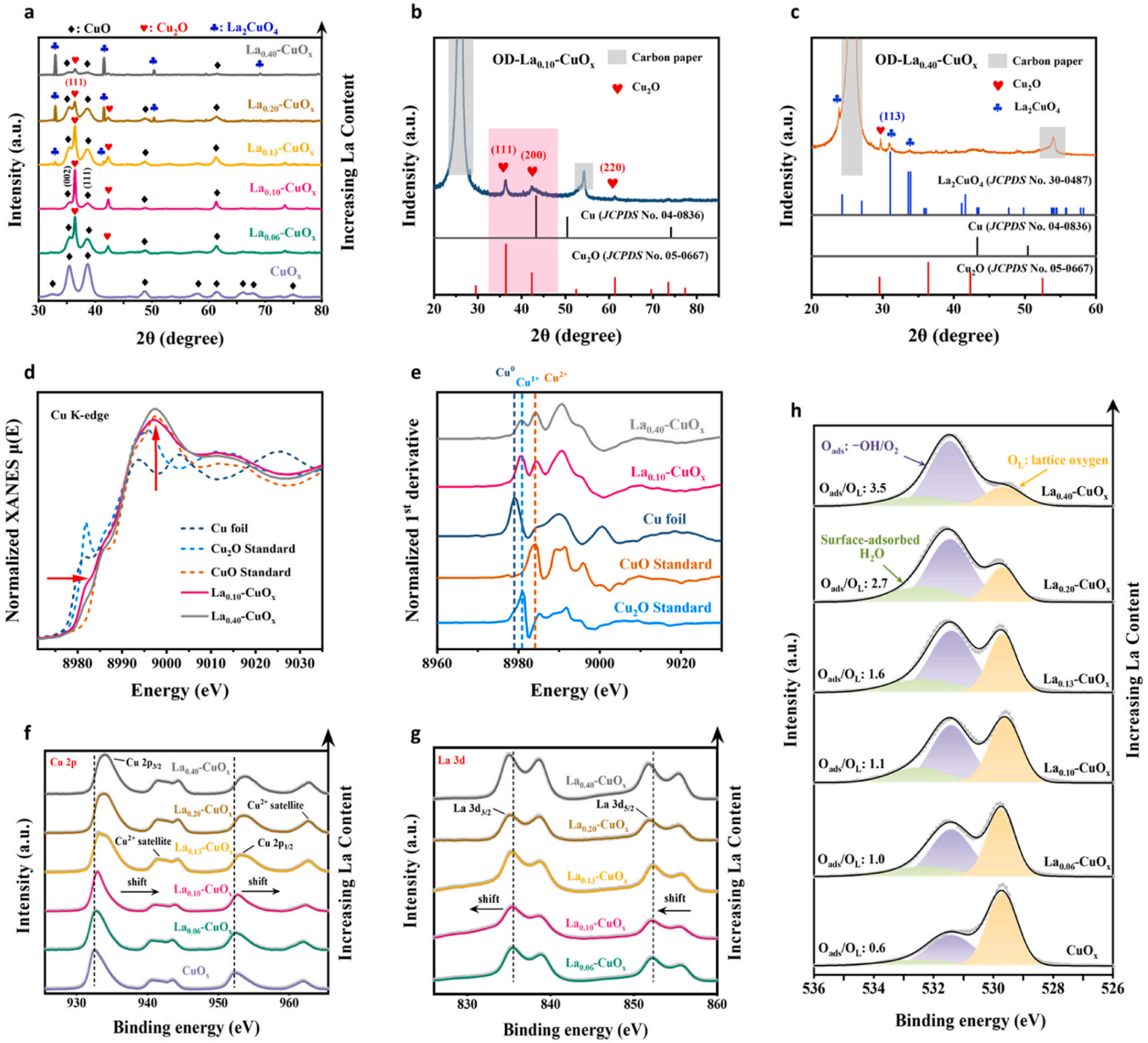

Fig. 2. a) XRD patterns of CuO_x and various La-CuO_x catalysts prior to CO_2RR. The XRD patterns of b) OD-$La_{0.10}$-CuO_x and c) OD-$La_{0.40}$-CuO_x after CO_2RR at 300 mA cm^{-2} for 30 minutes in 1 M KCl and 1 M KOH, respectively. d) Normalized intensity and e) First-order derivative of Cu K-edge X-ray absorption near edge structure (XANES spectra for $La_{0.10}$-CuO_x, $La_{0.40}$-CuO_x and other reference standards. High-resolution XPS spectra of f) Cu 2p, g) La 3d, and h) O 1 s of CuO_x and the as-prepared La-CuO_x catalysts.

doping, which has been reported to effectively prevent lattice oxygen leaching, thereby stabilizing Cu^+ species and maintaining the Cu_2O phase [37–40]. The diffraction patterns of OD-$La_{0.40}$-CuO_x were also examined at various electrolysis duration in 1 M KOH at a current density of 400 mA cm^{-2}. The crystalline phases in OD-$La_{0.40}$-CuO_x, comprising La_2CuO_4 and Cu_2O, remain stable throughout electrolysis, although the proportion of the Cu_2O phase decreases after 30 minutes (Figs. 2**c and** S11c). Additionally, ex situ Cu LMM Auger spectra of the reconstructed OD-CuO_x, OD-$La_{0.10}$-CuO_x, and OD-$La_{0.40}$-CuO_x were gathered under identical conditions as ex situ XRD tests to elucidate the Cu oxidation states. During CO_2RR, OD-CuO_x shows an increasing proportion of Cu^0 species (918.4 eV) over 10-min increments, which fully occupies by 30 and 60 minutes (Fig. S13a). Conversely, the Cu LMM spectra for OD-$La_{0.10}$-CuO_x indicate a stabilization of Cu^+ species (916.8 eV) during 60 minutes of CO_2 electrolysis (Fig. S13b). Furthermore, the spectra for OD-$La_{0.40}$-CuO_x reveal a mixture of Cu^+ (916.8 eV) and Cu^{2+} (917.8) species both before and after various electrolysis intervals (Fig. S13**c**). Notably, the ex situ X-ray photoelectron spectroscopy (XPS) of La 3d spectra reveals that La^{3+} species remain unchanged in both OD-$La_{0.10}$-CuO_x and OD-$La_{0.40}$-CuO_x during 60 minutes of CO_2 electrolysis. As illustrated in Fig. S14, peaks at 838.8 eV and 855.6 eV correspond to La^{3+} $3d_{5/2}$ and $3d_{3/2}$, respectively. The spin-orbit splitting energy of 16.8 eV between the $3d_{5/2}$ and $3d_{3/2}$ states of La^{3+} is consistent with reported values for La_2O_3 [41].

To further identify the Cu oxidation state and microstructure of localized Cu species, X-ray absorption spectroscopy (XAS) was conducted at the Cu K-edge for $La_{0.10}$-CuO_x, $La_{0.40}$-CuO_x and reference standards (Cu, Cu_2O and CuO). As shown in Fig. 2**d**, the absorption edges of $La_{0.10}$-CuO_x and $La_{0.40}$-CuO_x in the normalized Cu K-edge X-ray absorption near edge structure (XANES) are positioned between those of the Cu_2O and CuO standards, indicating Cu valence states between +1 and +2 for both samples. This finding aligns with XRD results, showing that $La_{0.10}$-CuO_x and $La_{0.40}$-CuO_x possess mixed phases of Cu_2O, CuO and La_2CuO_4. Furthermore, the white-line intensity of $La_{0.40}$-CuO_x surpasses that of the CuO standard and $La_{0.10}$-CuO_x, implying a higher oxidation state of Cu in $La_{0.40}$-Cu. The normalized first-order derivative of XANES for $La_{0.10}$-CuO_x and $La_{0.40}$-CuO_x display peaks overlapping with Cu_2O and CuO at approximately 8980 eV and 8984 eV, verifying the existence of Cu(I) and Cu(II) species in $La_{0.10}$-CuO_x and $La_{0.40}$-CuO_x (Fig. 2**e**). In conjunction with XRD analysis, the Cu(II) species in $La_{0.40}$-CuO_x mainly derive from the La_2CuO_4 phase.

High-resolution XPS was employed to investigate electronic interactions between Cu and La and to determine the surface chemical states of elements in the as-prepared catalysts. As expected, the full XPS spectra confirmed the presence of Cu, La and O, aligning with the EDS analysis of the La-CuO_x catalysts (Fig. S15**)**. With increased La doping, there is a marked reduction in peak intensity of Cu 2p, whereas that for La 3d rises. Fig. 2**f** depicts the core-level XPS spectra of Cu 2p for CuO_x, $La_{0.10}$-CuO_x, and other La-CuO_x catalysts with different La doping levels. Notably, the Cu $2p_{3/2}$ and Cu $2p_{1/2}$ peaks in the La-CuO_x catalysts shift to higher binding energies with increased La doping compared to CuO_x peaks. This suggests charge transfer from Cu to La, attributed to the unique electronic structure of La's unfilled 4 f orbitals [40]. Furthermore, strong Cu^{2+} satellite peaks, present in all samples, range between 940 eV and 945 eV, indicating either CuO or La_2CuO_4 phases, as supported by XRD analysis. Additionally, the peaks located between 917.8 eV and 916.8 eV in the Cu LMM spectra confirm the presence of Cu^{2+} and Cu^+ species (Fig. S16). This finding aligns with the XRD results (Fig. 2**a**) discussed earlier. Similarly, the core-level XPS spectra of La 3d (Fig. 2**g**) show significant shifts of La $3d_{3/2}$ and La $3d_{5/2}$ peaks to lower energy with increased La content, suggesting electron transfer from Cu to La, which corroborates the findings from the Cu 2p XPS analysis and highlights favorable charge transfer within the La-CuO_x catalyst system.

To further explore the distribution of oxygen species in La-CuO_x catalysts, the O 1 s spectra of the as-prepared La-CuO_x catalysts were examined via XPS. As shown in Fig. 2**h**, the asymmetric O 1 s peaks indicate the presence of different oxygen species, which deconvolute into three peaks at binding energies of 529.7, 531.5 and 532.7 eV, respectively. The peak at 529.7 eV corresponds to the lattice oxygen (O_L) within the Cu-O-Cu and Cu-O-La bonds [42,43]. The peaks at 531.5 and 532.7 eV are attributed to surface-adsorbed hydroxyl or oxygen species (−OH/O_2, O_{ads}) and surface-adsorbed H_2O on the La-CuO_x matrix, respectively [44,45]. Comparing the O_{ads} to O_L ratio reveals La doping markedly increases the proportion of surface-adsorbed −OH/O_2, elevating the ratio from 0.6 to 3.5. XPS results demonstrate that the La-CuO_x catalysts, fabricated through this one-pot thermal process, are rich in surface-adsorbed hydroxyl or oxygen species. Prior studies indicate that surface oxygen-containing species play a role in stabilizing reaction intermediates for enhanced CO_2RR performance [46].

3.2. *Electrochemical performance of CO_2RR*

The electrocatalytic CO_2RR performance of oxide-derived CuO_x and La-CuO_x catalysts was evaluated in a custom liquid electrolyte flow cell under constant current densities in the range of 100–500 mA cm^{-2} (Fig. S17). Unless otherwise specified, potentials were converted to the reversible hydrogen electrode (RHE) scale using an 85% *iR* correction to minimize the variations between the actual and desired potential at high current densities. The catholyte consisted of 1 M KOH and 1 M KCl solutions to evaluate the electrocatalysts' performance at industrial current densities in both alkaline and neutral electrolytes, respectively. Prior to each on-line GC test, air-tightness checks, cyclic voltammetry (CV) activation, and gas outlet flow rate tests were performed.

To assess the selectivity towards C_2H_4, Faradaic efficiencies (FEs) for the synthesized OD-CuO_x and $La_{0.10}$-CuO_x were evaluated in alkaline and neutral electrolytes across current densities of 100 to 500 mA cm^{-2}. As shown in Fig. 3**a**, the CuO_x catalyst with its ultrasmall particle size exhibits a gradual increase in C_2H_4 selectivity with rising cathodic current density, achieving a maximum FE_{C2H4} of about 40%. In contrast, the OD-$La_{0.10}$-CuO_x shows enhanced FE_{C2H4} in both electrolyte types across the same current density range. It achieves up to 52% FE_{C2H4} in 1 M KCl at a current density of 300 mA cm^{-2}. The use of neutral electrolytes significantly mitigates challenges related to (bi)carbonate precipitation and gas diffusion electrode (GDE) collapse, thus enabling efficient and stable electrolysis at high current densities [47,48]. To investigate the impact of La doping on electron selectivity in CO_2RR-to-C_2H_4, chronopotentiometry tests were conducted on CuO_x and La-CuO_x catalysts in both 1 M KOH and KCl solutions at a current density of 300 mA cm^{-2}. Fig. 3**b** illustrates a notable increase in FE_{C2H4} with greater La content, peaking at OD-$La_{0.10}$-CuO_x. CO_2RR-to-C_2H_4 performance diminishes sharply with further La content increase, as observed in OD-$La_{0.13}$-CuO_x and beyond. Notably, for OD-$La_{0.40}$-CuO_x, FE_{C2H4} drops to 1.5% and 1.7% in 1 M KOH and 1 M KCl, respectively (Fig. S18 and S19). This electron selectivity towards CH_4 can be attributed to the emergence of La_2CuO_4 phase, progressively replacing the initial mixed phase of OD-$La_{0.10}$-CuO_x (Fig. 2**a**), aligning with the finding reported in a previous work [43]. Detailed gas product distribution data for each sample at different current densities and in different electrolytes, along with the Faradaic efficiency of gas and liquid products for OD-$La_{0.10}$-CuO_x in 1 M KCl and OD-$La_{0.40}$-CuO_x in 1 M KOH at current densities ranging from 100 to 500 mA cm^{-2}, are provided in Tables S2-S6.

To gain insights into C_{2+} product formation selectivity, the focus is placed on OD-$La_{0.10}$-CuO_x, which demonstrates the highest CO_2RR-to-C_2H_4 selectivity in 1 M KCl at 300 mA cm^{-2}. The FEs for various gas/liquid products over OD-$La_{0.10}$-CuO_x are compared in Fig. S20 to evaluate CO_2RR-to-C_{2+} performance. Even at high current densities (300 mA cm^{-2}), OD-$La_{0.10}$-CuO_x achieves an FE exceeding 80% for C_{2+} products (Fig. 3**c)** via CO_2 electroreduction, comprising 51.8% FE_{C2H4}, 21.5% FE_{C2H5OH}, and 7.1% $FE_{n\text{-}propanol}$ (Fig. S20 and Table S4). This impressive performance is attributed to the suppression of the competing HER. The FE of HER is limited to approximately 10% at current densities between 200 and 400 mA cm^{-2} (Fig. S20). Moreover,

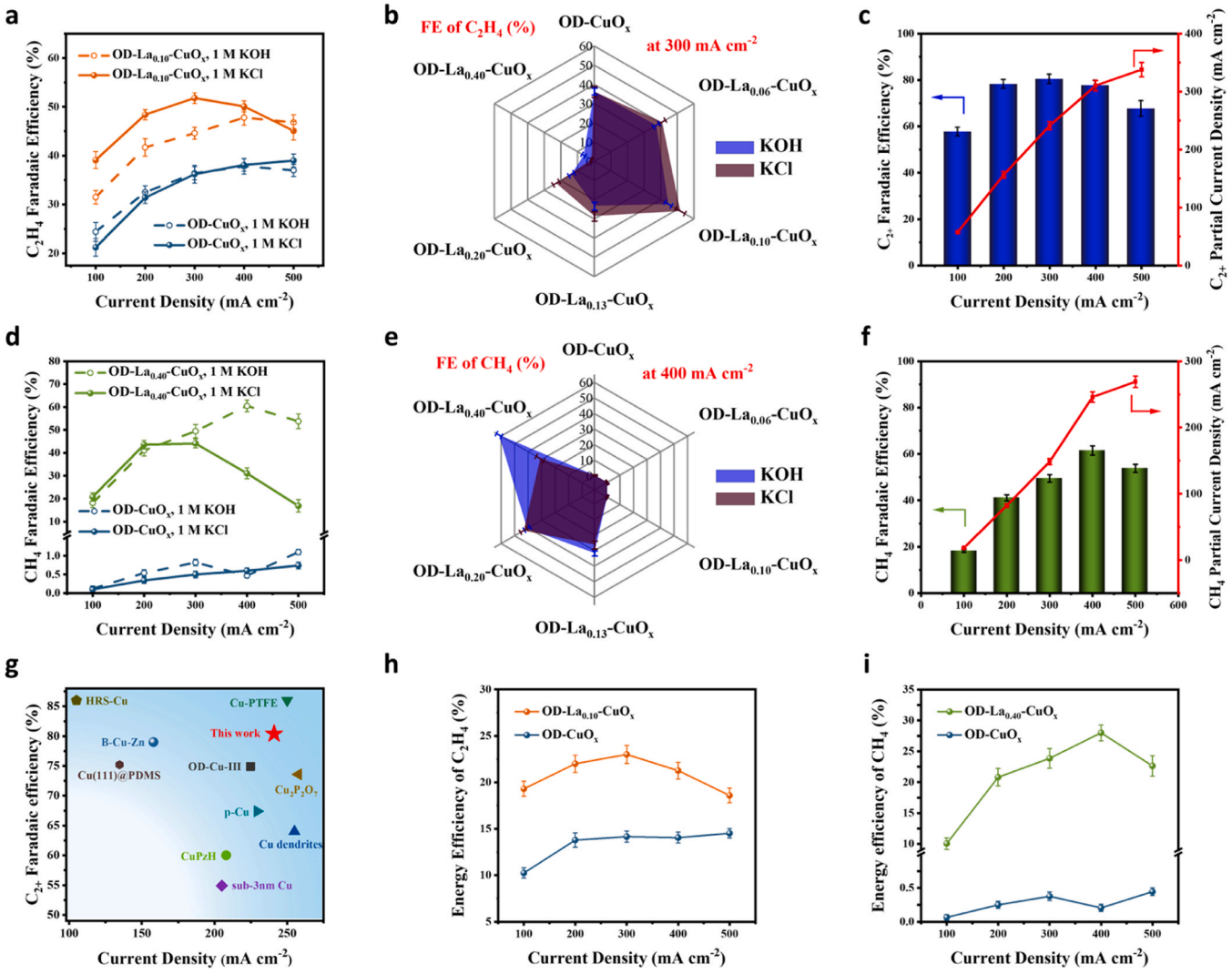

Fig. 3. Performance on CO_2RR to C_{2+} products and CH_4 in a flow cell. a) FE of C_2H_4 on OD-$La_{0.10}$-CuO_x and OD-CuO_x in 1 M KOH and 1 M KCl at current densities from 100 to 500 mA cm^{-2}. b) FE of C_2H_4 on OD-CuO_x and OD-La-CuO_x catalysts at 300 mA cm^{-2} in 1 M KOH and 1 M KCl; c) FE and partial current densities of C_{2+} products for OD-$La_{0.10}$-CuO_x in 1 M KCl at varying current densities; d) FE of CH_4 on OD-CuO_x and OD-$La_{0.40}$-CuO_x in 1 M KOH and 1 M KCl at current densities from 100 to 500 mA cm^{-2}; e) FE of CH_4 on OD-CuO_x and various OD-La-CuO_x catalysts at 400 mA cm^{-2} in 1 M KOH and 1 M KCl; f) FE and partial current densities of CH_4 for OD-$La_{0.40}$-CuO_x in 1 M KOH under different current densities. g) Comparison of the FE_{C2+} value of OD-$La_{0.10}$-CuO_x in this work with other reported high-performance Cu-based electrocatalysts [49–60]. h) Cathodic energy efficiency of C_2H_4 on OD-$La_{0.10}$-CuO_x and OD-CuO_x in 1 M KCl, and i) Cathodic energy efficiency of CH_4 on OD-$La_{0.40}$-CuO_x and OD-CuO_x in 1 M KOH, at current densities from 100 to 500 mA cm^{-2}.

the rich grain boundaries in OD-$La_{0.10}$-CuO_x (Fig. S6) are likely to enhance C-C coupling by improving *CO adsorption and H_2O dissociation, thereby facilitating CO_2RR to C_{2+} products [30]. OD-$La_{0.10}$-CuO_x also demonstrates superior CO_2RR-to-C_{2+} performance in a neutral electrolyte, reaching C_{2+} partial current densities near 350 mA cm^{-2} (Fig. 3**c**).

Beyond achieving excellent C_{2+} selectivity, the emergence of the La_2CuO_4 phase and its structure-function relationships with CO_2RR-to-CH_4 are of great interest. Consequently, online FE tests were conducted at 100–500 mA cm^{-2} in both electrolytes to assess the effect of La_2CuO_4 phase on FE_{CH4} (Figs. S18 and S19). Notably, OD-$La_{0.40}$-CuO_x exhibits no less than 40% FE_{CH4} at current densities of 200–500 mA cm^{-2} in 1 M KOH (Fig. 3**d**). However, undoped OD-CuO_x shows almost no FE_{CH4}, achieving less than 1% in both alkaline and neutral electrolytes. FE_{CH4} was further examined for CuO_x and La-CuO_x catalysts at 400 mA cm^{-2} in 1 M KOH. As illustrated in Fig. 3**e**, catalysts containing La_2CuO_4 phase (ranging from OD-$La_{0.13}$-CuO_x to OD-$La_{0.40}$-CuO_x) significantly promote CO_2 hydrogenation to CH_4, especially in alkaline environments. OD-$La_{0.40}$-CuO_x achieves up to 61.5% FE_{CH4} at 400 mA cm^{-2} in 1 M KOH, with partial current densities reaching up to 270 mA cm^{-2} (Fig. 3**f**). This can be attributed to the increased La_2CuO_4 ratio and surface-adsorbed oxygen-containing species, which are considered to provide H_2O dissociation sites to enhance CO_2RR-to-CH_4 process [30,61]. However, with further increase in La content, the highest FE_{CH4} achieved by OD-$La_{0.50}$-CuO_x is below 40% in both 1 M KOH and 1 M KCl, accompanied by serious hydrogen evolution reaction (Tables S5 and S6). Besides, comparing alkaline and neutral electrolytes, FE_{H2} analysis for OD-$La_{0.40}$-CuO_x indicates that HER is boosted in neutral 1 M KCl, reducing CH_4 selectivity (Fig. S21).

In summary, the OD-$La_{0.10}$-CuO_x and OD-$La_{0.40}$-CuO_x catalysts demonstrate high electron selectivity for producing C_2H_4 and CH_4, respectively. As shown in Fig. 3**g and** S22**,** these electrocatalysts surpass the performance of most reported state-of-the-art Cu-based catalysts for CO_2RR-to-C_{2+} and CO_2RR-to-CH_4 in a gas-fed flow cell configuration, respectively. The original data supporting these findings are detailed in Tables S7 and S8. Energy efficiency and electrocatalyst stability remain challenges in the CO_2RR process [62]. Accordingly, the as-prepared electrocatalysts (OD-$La_{0.10}$-CuO_x and OD-$La_{0.40}$-CuO_x) were integrated

into a gas-fed flow cell with 1 M KCl and 1 M KOH as electrolytes, and nickel foam as the anode, to evaluate their energy efficiency and stability. As shown in Fig. 3**h** and **i,** at 300 and 400 mA cm^{-2}, the highest cathodic energy efficiencies for C_2H_4 and CH_4 of 23.0% and 28.2% are achieved on OD-$La_{0.10}$-CuO_x and OD-$La_{0.40}$-CuO_x, respectively, exceeding recent reports of 20.9% for C_2H_4 [63] and 20% for CH_4 [64]. Detailed current density, Faradic efficiency, cathodic energy efficiency, and applied potential post-*iR* compensation for OD-CuO_x and

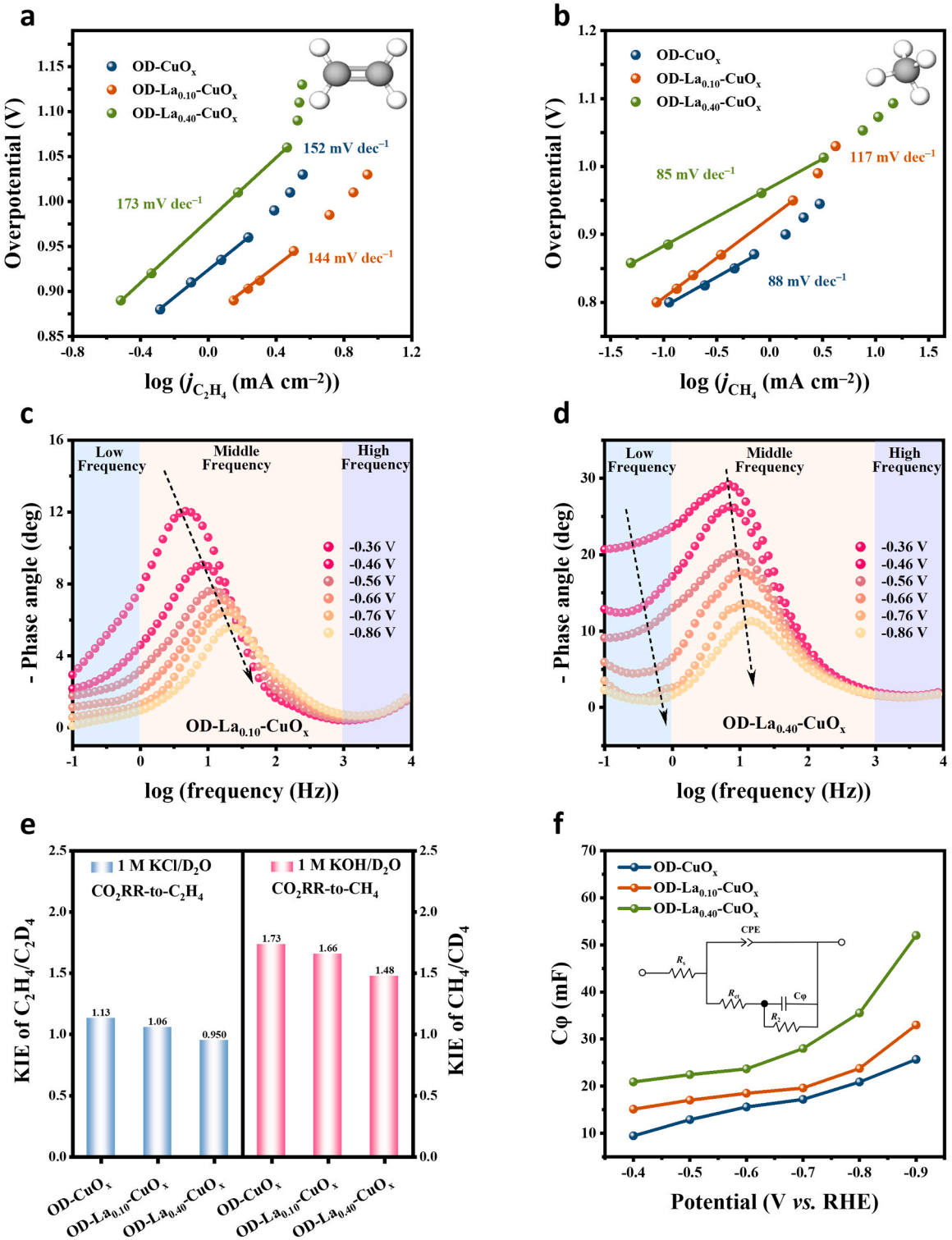

Fig. 4. Tafel plots of the formation of a) C_2H_4 in 1 M KCl, and b) CH_4 in 1 M KOH for OD-CuO_x, OD-$La_{0.10}$-CuO_x, and OD-$La_{0.40}$-CuO_x. Bode phase plots of c) OD-$La_{0.10}$-CuO_x in 1 M KCl and d) OD-$La_{0.40}$-CuO_x in 1 M KOH at the equilibrium potential for CO_2 electrolysis. e) Kinetic isotope effect (KIE) values for CO_2RR-to-C_2H_4 on OD-CuO_x and OD-$La_{0.10}$-CuO_x measured at 300 mA cm^{-2} in 1 M KCl (left) and KIE values for CO_2RR-to-CH_4 on OD-CuO_x and OD-$La_{0.40}$-CuO_x measured at 400 mA cm^{-2} in 1 M KOH (right). f) Plots of calculated proton-adsorption pseudo-capacitance (Cφ) for OD-CuO_x, OD-$La_{0.10}$-CuO_x, and OD-$La_{0.40}$-CuO_x at different potentials in 1 M KOH, with inset showing the equivalent circuit for the single-adsorbate mechanism (R_s: solution resistance; R_{ct}: charge transfer resistance; R_2: hydrogen adsorption resistance; CPE: constant phase angle element).

OD-$La_{0.10}$-CuO_x in 1 M KCl and OD-CuO_x and OD-$La_{0.40}$-CuO_x in 1 M KOH are provided in Tables S9 and S10, respectively. Moreover, OD-$La_{0.10}$-CuO_x shows stable CO_2RR-to-C_2H_4 operation for 16 hours at 300 mA cm^{-2} in 1 M KCl with a cation exchange membrane. As illustrated in Fig. S23, there is only a slight decrease in FE_{C2H4} during the stability test, indicating excellent CO_2RR stability. The spent OD-$La_{0.10}$-CuO_x catalyst reaches its highest FE_{C2H4} at around 30 minutes and maintains 90% of the highest electron selectivity ($FE_{C2H4} > 45\%$) in subsequent runs in a flow cell. OD-$La_{0.40}$-CuO_x sustains stable CO_2RR-to-CH_4 operation for 8 hours at 400 mA cm^{-2} in 1 M KOH with an anion exchange membrane. As shown in **Fig. S24**, despite the hydrophilic nature of OD-$La_{0.40}$-CuO_x causing slight fluctuations in the applied potential range, it achieves the highest FE_{CH4} at around 30 minutes and maintains FE_{CH4} over 50% during the first 6 hours. After 8 hours of catalyst stability testing, the gas diffusion electrode (GDE) shows (bi) carbonate precipitation and flooding issues, leading to the blockage of the gas transfer channel in the flow cell, which reduces the electron selectivity for CH_4.

3.3. Kinetic insights into CO_2RR

Electrocatalytic kinetic analysis is a well-established approach for investigating reaction mechanisms and determining the structure-function relationships of electrocatalysts. To elucidate the kinetics underlying the enhanced CO_2RR-to-C_2H_4/CH_4 performance of various OD-La-CuO_x catalysts, Tafel curves for the formation of C_2H_4 and CH_4 at different partial current densities were plotted. During the CO_2RR-to-C_2H_4 process, the Tafel slope for OD-$La_{0.10}$-CuO_x in 1 M KCl (144 mV dec^{-1}) is lower than that of undoped OD-CuO_x (152 mV dec^{-1}) and OD-$La_{0.40}$-CuO_x (173 mV dec^{-1}), the latter being enriched with La_2CuO_4 phases due to the increased La doping (Fig. 4**a**). A similar trend was observed in 1 M KOH, indicating that OD-$La_{0.10}$-CuO_x has superior initial activity and kinetics for efficient C_2H_4 production (Fig. S25a). Furthermore, kinetic analysis of the CO_2RR-to-CH_4 process reveals that the Tafel slope for OD-$La_{0.40}$-CuO_x in 1 M KOH is 85 mV dec^{-1}, lower than that of OD-CuO_x (88 mV dec^{-1}) and OD-$La_{0.10}$-CuO_x (117 mV dec^{-1}) (Fig. 4**b**). OD-$La_{0.40}$-CuO_x also exhibits the lowest Tafel slope in 1 M KCl, indicating enhanced electrocatalytic activity, primarily due to accelerated electron transfer from the electrode to catalyst during CO_2 methanation (Fig. S25b).

Moreover, *in situ* electrochemical impedance spectroscopy (EIS) was employed to assess the electrocatalytic kinetics and ion diffusion capabilities. Figs. 4**c, d and** S26 show the frequency-dependent changes in the Bode phase plots for OD-$La_{0.10}$-CuO_x and OD-$La_{0.40}$-CuO_x under various applied potentials. Generally, the Bode plots show a shift of the phase angle (φ) towards higher frequency regions with increasing applied potential, along with a reduction in the peak value. This results in a decrease in Faradaic resistance and an increase in surface reaction rate, aligning with the electrocatalytic processes occurring on the surface [65,66]. The Bode plot reveals a more substantial decline in phase angles for OD-$La_{0.40}$-CuO_x compared to OD-$La_{0.10}$-CuO_x in both 1 M KCl (Figs. 4**c and** S26**b**) and 1 M KOH (Figs. 4**d and** S26a) when subjected to applied potentials from −0.36 to −0.86 V. This suggests that the surface of OD-$La_{0.40}$-CuO_x is more conducive to enhanced charge transfer capability and superior electronic conductivity [67]. As previously analyzed by XPS, this may be attributed to enriched surface oxygen-containing species in OD-$La_{0.40}$-CuO_x (Fig. 2**h**).

In this work, KOH and KCl electrolytes were applied in the electrocatalytic CO_2RR processes, thus anticipating *H donation primarily from H_2O dissociation rather than HCO_3^- [21]. To understand the role of H_2O dissociation and *H transfer in the CO_2RR-to-C_{2+}/CH_4 processes, we examined the kinetic isotope effect (KIE) of hydrogen/deuterium (H/D) on OD-CuO_x, OD-$La_{0.140}$-CuO_x, and OD-$La_{0.40}$-CuO_x. The KIE value for H/D is determined by the ratio of the formation rates of the product before and after substituting H_2O with D_2O in the original electrolyte (Eq. S5). Generally, higher KIE values indicates more pronounced effects of H_2O dissociation and *H transfer in the rate-determining step (RDS). Typically, KIE values exceeding 1 indicate that H_2O activation and proton transfer are involved in the RDS [68]. A KIE value greater than 1.5 suggests that *H attraction significantly affects the reaction rate [69,70].

To determine the KIE value of C_2H_4, D_2O was used instead of H_2O in the 1 M KCl electrolyte. As shown in Fig. 4**e**, the KIE values of C_2H_4 for OD-CuO_x, OD-$La_{0.10}$-CuO_x, and OD-$La_{0.40}$-CuO_x are around 1, specifically 1.13, 1.06 and 0.950, respectively, suggesting there may be no *H-related RDS or multiple parallel *H-related RDSs in C_2H_4 formation mechanisms [68]. In addition, the KIE value of C_2H_4/C_2D_4 for OD-$La_{0.40}$-CuO_x is the lowest compared to OD-CuO_x and OD-$La_{0.10}$-CuO_x, confirming that the presence of La accelerates H_2O dissociation to provide *H for CO_2RR-to-C_2H_4. Similarly, by using D_2O instead of H_2O in 1 M KOH, the KIE values of CH_4 on OD-CuO_x, OD-$La_{0.10}$-CuO_x, and OD-$La_{0.40}$-CuO_x are 1.73, 1.66 and 1.48, respectively. This suggests that the CO_2RR-to-CH_4 kinetics on OD-$La_{0.40}$-CuO_x is significantly constrained by *H transfer, as shown in Fig. 4**e**.

Given the well-established effects of H_2O dissociation and protonation on the kinetics of CO_2RR-to-C_{2+}/CH_4, we subsequently investigated the coverage of adsorbed *H on the catalyst surface using an equivalent circuit for a single-adsorbate mechanism (Armstrong's electric circuit) via *in situ* EIS measurements [71]. The proton-adsorption pseudo-capacitance (Cφ) in the second parallel component represents the *H coverage [11,71,72]. As illustrated in Figs. 4**f and** S27, Cφ for OD-$La_{0.40}$-CuO_x exceeds that of OD-$La_{0.10}$-CuO_x and OD-CuO_x across the same applied potential range (−0.4 to −0.9 V vs. RHE) in both 1 M KOH and 1 M KCl. This indicates that OD-$La_{0.40}$-CuO_x, with its high H_2O dissociation activity, can provide sufficient *H for the multistep protonation of CH_4 intermediates. Given that Cφ increases with rising La content, it is confirmed that doped-La favors proton delivery in CO_2RR, consistent with the results from the above KIE experiment.

3.4. In situ ATR-SEIRAS observations of CO_2RR

To explore the mechanisms of dimerization and hydrogenation during CO_2RR on the as-prepared OD-La-CuO_x catalysts, time-resolved *in situ* ATR-SEIRAS was employed to monitor the formation of various intermediates on OD-CuO_x control, OD-$La_{0.10}$-CuO_x, and OD-$La_{0.40}$-CuO_x, focusing on the pathways leading to C_1 and C_{2+} products. Fig. 5**a** illustrates the observed states of surface intermediates on undoped OD-CuO_x nanoparticles during a continuous 10-minute chronoamperometry test. The absorption peak at 1260 cm^{-1}, corresponding to the C═O stretching in the carboxylate radical (*COOH), intensifies with prolonged electrolysis [73]. The OD-CuO_x sample exhibits a distinct signal for the CO vibrational frequency (νCO) in *OCCOH at 1460 cm^{-1}, indicative of the intermediate in C_{2+} product formation [18]. Interestingly, a peak at 1556 cm^{-1} indicates the presence of *OCCHO, a key intermediate in C_2H_4 formation along with *OCCOH [74]. The IR band at 1640 cm^{-1} is commonly associated with the bending mode of the H_2O molecule (H-O-H) [18]. These observations are consistent with the CO_2RR product distribution for the OD-CuO_x control.

Further analysis of the surface intermediate states was conducted using OD-$La_{0.10}$-CuO_x under identical *in situ* ATR-SEIRAS conditions (Fig. 5**b**). Continuous chronoamperometry reveals the same distinct absorption peaks near 1260 cm^{-1} and 1642 cm^{-1}, originating from *COOH and *H_2O, respectively [18,73]. Notably, a broad peak ranging from 1400 to 1470 cm^{-1} is primarily composed of two peaks at 1410 cm^{-1} and 1445 cm^{-1}, which correspond to the symmetric stretching of *COO^- and *C_2H_4, respectively [75,76]. The observed *C_2H_4 reaction intermediates indicate the formation of C_2H_4 on OD-$La_{0.10}$-CuO_x. With continued electrolysis, a peak at 1500 cm^{-1} appears, attributed to *OCCO [18]. Additionally, another time-dependent IR peak is detected at 1550 cm^{-1}, which is attributed to adsorbed *OCCHO [74]. By comparing the intensities of both *OCCO and *OCCHO peaks, we find that *OCCHO dominates the C-C coupling

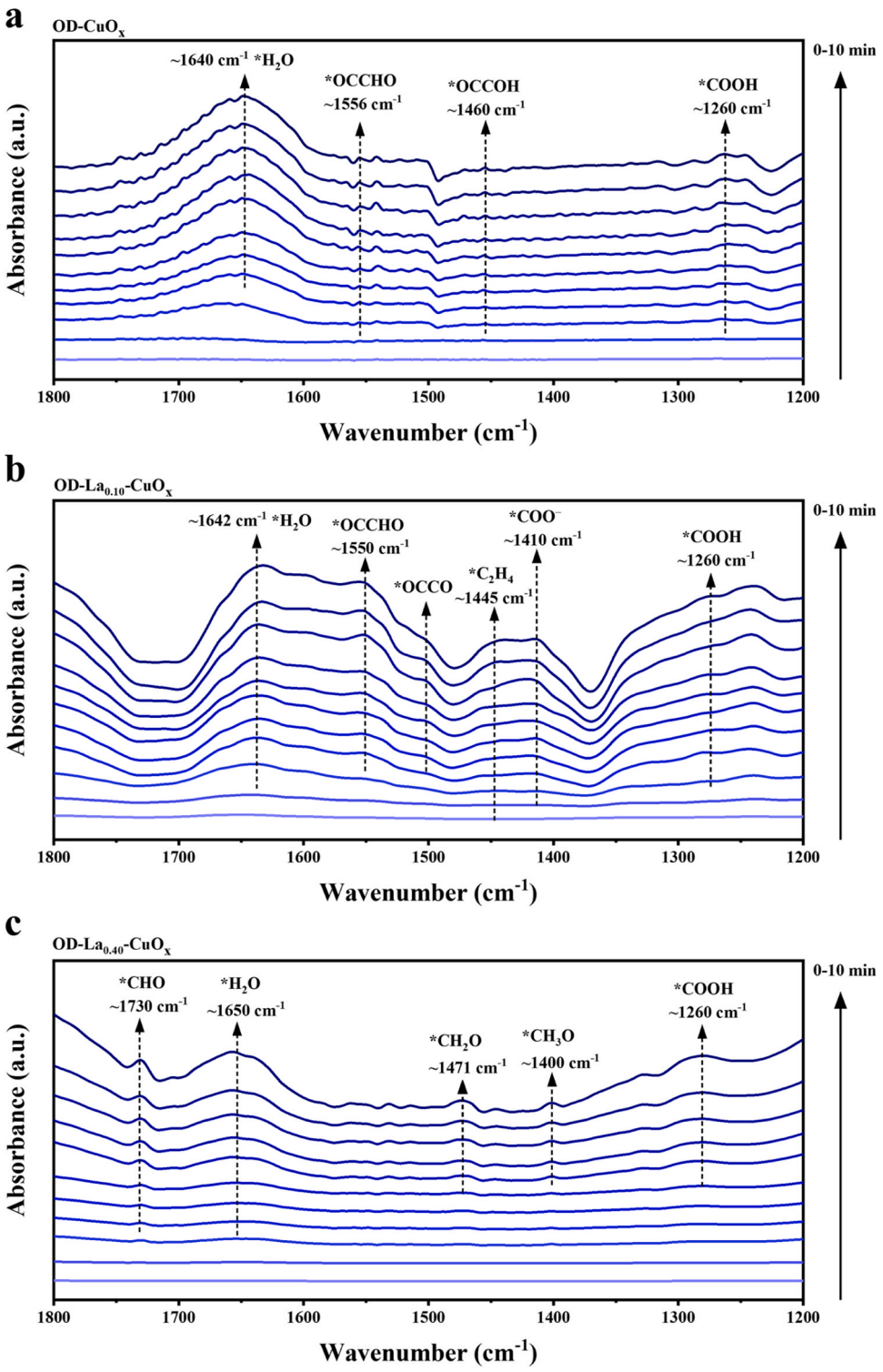

Fig. 5. Time-dependent electrochemical *in situ* ATR-SEIRAS measurements of a) OD-CuO_x, b) OD-$La_{0.10}$-CuO_x, and c) OD-$La_{0.40}$-CuO_x at a potential of −0.8 V vs. RHE. All spectroscopic tests were conducted in a CO_2-saturated 1 M KCl solution over 10-min CO_2 electrolysis.

process on OD-$La_{0.10}$-CuO_x. These results confirm that the surface of OD-$La_{0.10}$-CuO_x is predominantly covered with intermediates crucial for C_{2+} product formation, such as *C_2H_4, *OCCO, and *OCCHO. The increasing intensity of these peaks with ongoing electrolysis strongly corroborates the excellent performance for CO_2RR-to-C_{2+} discussed earlier.

To further substantiate that varying La-Cu ratios influence product selectivity, *in situ* time-dependent ATR-SEIRAS tests were also performed on OD-$La_{0.40}$-CuO_x. A peak associate with *COOH is found at 1260 cm^{-1} [73]. Interestingly, signals indicative of intermediates for C_{2+} formation (*OCCHO, *OCCO, and *OCCOH) are weakened or even absent (Fig. 5**c**). Instead, a peak at 1730 cm^{-1} arises from the C═O stretching of *CHO, a critical intermediate in the CO_2RR-to-CH_4 pathway [77]. Moreover, a distinct *CH_2O signal appears at 1471 cm^{-1} from the protonation of *CHO [78]. Additionally, a peak corresponding to *CH_3O is detected at 1400 cm^{-1}, produced from further protonation

of *CH_2O and serving as a crucial intermediate of electrochemical CO_2 methanation [78]. Throughout constant electrolysis, a prominent broad peak emerges in the IR range of 1600–1700 cm^{-1}, particularly around 1650 cm^{-1}, related to the H-O-H bending mode of H_2O molecules [18]. As mentioned above, this broad peak suggests the concurrent activation of H_2O on the $La_{0.40}$-Cu surface during CO_2RR. Based on the intermediate information obtained from OD-$La_{0.40}$-CuO_x, it can be speculated that the adsorbed H_2O molecules continuously supply protons, enhancing the protonation of intermediates, promoting *CHO, *CH_2O, and *CH_3O formation, and optimizing CO_2RR kinetics [79]. In summary, the results of *in situ* ATR-SEIRAS depicted in Fig. 5**c** demonstrate minimal amounts of intermediates for C_{2+} product formation on OD-$La_{0.40}$-CuO_x, but a substantial accumulation of intermediates related to CH_4, which is consistent with observations in product distribution of electrochemical experiments.

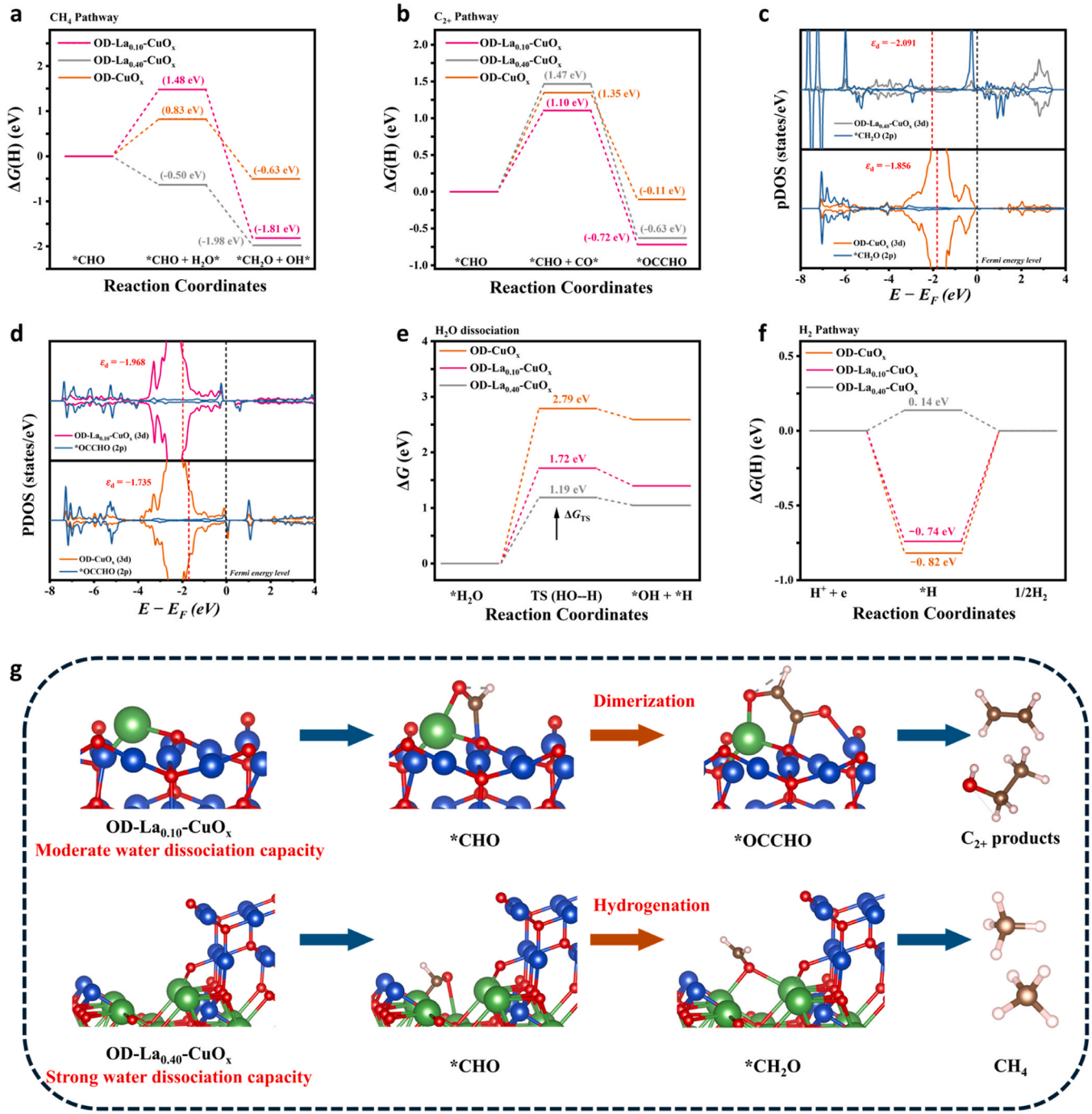

Fig. 6. a) Gibbs free energy diagrams for the hydrogenation of *CHO to *CH_2O on OD-CuO_x surfaces without La doping and on OD-$La_{0.40}$-CuO_x; b) Gibbs free energy diagrams for the dimerization of *CHO to *OCCHO on OD-CuO_x surfaces without La doping and on OD-$La_{0.10}$-CuO_x; c&d) Projected density of states (PDOS) of d orbitals associated with *CH_2O and *OCCHO on OD-$La_{0.40}$-CuO_x and OD-$La_{0.10}$-CuO_x, respectively, with d-band centers (ε_d) indicated by red dashed lines. Adsorption energy diagram of (e) H_2O dissociation and (f) hydrogen ad-desorption for OD-CuO_x without La doping, OD-$La_{0.40}$-CuO_x and OD-$La_{0.10}$-CuO_x. (g) Proposed reaction mechanisms, illustrating CO_2 dimerization to C_{2+} products on OD-$La_{0.10}$-CuO_x (top) and CO_2 hydrogenation to CH_4 on OD-$La_{0.40}$-CuO_x (bottom). Atoms are colored as follows: Cu, blue; La, green; O, red; C, brown; and H, pale pink.

3.5. DFT calculations of CO_2RR

To elucidate the reaction mechanisms and product correlations of La-CuO_x catalysts with varying levels of La doping in CO_2RR, DFT calculations at the functional/basis level were performed. Based on the structural characteristics observed from the XRD patterns of the La-CuO_x catalysts post-reaction (Fig. 2**b** and **c**), theoretical models of OD-CuO_x without La doping, OD-$La_{0.10}$-CuO_x, and OD-$La_{0.40}$-CuO_x were constructed (Fig. S28). Two primary reaction pathways for CO_2RR-to-CH_4 have been documented [80]: namely *CO → *CHO → *CH_2O → *CH_3O → CH_4 and *CO → *COH → *C → *CH → *CH_2 → *CH_3 → CH_4. To differentiate between these pathways, Gibbs free energy (ΔG) for *CO → *CHO and *CO → *COH transitions were calculated (Fig. S29). The results indicate that for all three electrocatalysts, the ΔG for *CO → *CHO is significantly lower than that for *CO → *COH, effectively ruling out the latter pathway as viable for CH_4 formation. Additionally, OD-$La_{0.10}$-CuO_x displays the lowest ΔG for *CO → *CHO compared to OD-CuO_x without La and OD-$La_{0.40}$-CuO_x, indicating the improved *CHO formation at moderate La doping levels. The subsequent analysis will prove why OD-$La_{0.40}$-CuO_x and OD-$La_{0.10}$-CuO_x exhibit enhanced selectivity towards CH_4 and C_{2+} products, respectively.

As illustrated in Fig. 6**a**, the CH_4 formation pathway (*CHO → *CH_2O) on OD-$La_{0.40}$-CuO_x is energetically more favorable (ΔG = −0.50 eV) than on OD-CuO_x without La doping (ΔG = 0.83 eV) and OD-$La_{0.10}$-CuO_x (ΔG = 1.48 eV). This suggests that intermediates conducive to CH_4 formation are more readily generated on OD-$La_{0.40}$-CuO_x. Furthermore, when comparing the reaction energy barriers for the CO_2RR-to-C_{2+} process among OD-$La_{0.10}$-CuO_x, OD-$La_{0.40}$-CuO_x, and OD-CuO_x (Fig. 6**b**), it is evident that the energy barrier for the *CHO → *OCCHO process on OD-$La_{0.10}$-CuO_x (1.10 eV) is lower than that of OD-CuO_x (1.35 eV) and OD-$La_{0.40}$-CuO_x (1.47 eV). This indicates that OD-$La_{0.10}$-CuO_x has optimal adsorption of *OCCHO. Three widely accepted C-C coupling pathways include CO-CO, CO-CHO and CO-COH [81]. Fig. S29 suggests that the CO-COH pathway is unlikely to occur due to a high energy barrier for *CO hydrogenation to form *COH. Additional comparisons of computed reaction energies between CO-CO and CO-CHO pathways (Fig. S30) indicate that the *OCCHO formation pathway is spontaneous for both OD-CuO_x without La doping and OD-$La_{0.10}$-CuO_x (−1.46 eV and −1.82 eV), with substantially lower energy barriers than those for the *OCCO formation pathway (1.76 eV and −0.60 eV), underscoring the dominance of the *CHO → *OCCHO pathway among the three C-C coupling routes. An examination of Gibbs free energy diagrams for CO_2RR-to-CH_4 and C_{2+} products reveals a close correlation between CO_2RR products on different OD-La-CuO_x catalysts and the divergence of *CHO and the formation of critical intermediates (i.e., *CH_2O and *OCCHO), which agrees with *in situ* ATR-SEIRAS observations (Fig. 5).

To understand the interactions between catalyst surfaces and key intermediates (*OCCHO/ *CH_2O) involved in forming C_{2+} products and CH_4, an analysis of the projected density of states (PDOS) was conducted. The PDOS illustrated in Fig. 6**c** and **d** reveal significant hybridization between the OD-$La_{0.40}$-CuO_x (3d) and *CH_2O (2p) orbitals, as well as between OD-$La_{0.10}$-CuO_x (3d) and *OCCHO (2p) orbitals, respectively. This implies robust binding interactions between the catalyst surfaces and these intermediates. Furthermore, the d-band centers (ε_d) of both OD-$La_{0.40}$-CuO_x and OD-$La_{0.10}$-CuO_x are situated further from the Fermi energy level (E_F = 0 eV) and are more negative compared to the CuO_x without La doping. This observation indicates that *OCCHO and *CH_2O exhibit weaker binding affinities and hence less resistance to desorption on OD-$La_{0.40}$-CuO_x and OD-$La_{0.10}$-CuO_x, thereby lowering the reaction barriers for CO_2 electroreduction to C_{2+} product and CH_4.

Inspired by the results of KIE and *in situ* EIS, we explored how adsorbed hydrogen (*H) affects the *CHO divergence. The concentration of *H on La-CuO_x catalysts featuring different hybridized heterostructures was determined by calculating the free energy changes associated with water dissociation ($\Delta G(H_2O)$) and hydrogen adsorption (ΔG(H)) on OD-CuO_x without La doping, OD-$La_{0.10}$-CuO_x and OD-$La_{0.40}$-CuO_x (Figs. S31–33). The $\Delta G(H_2O)$ value of OD-$La_{0.40}$-CuO_x is 1.19 eV, which is lower than that of OD-$La_{0.10}$-CuO_x (1.72 eV) and OD-CuO_x without La doping (2.79 eV) (Fig. 6**e**). This suggests that increased La doping enhances the thermodynamic favorability of H_2O dissociation in La-CuO_x catalysts, resulting in higher *H availability for the electrocatalytic process. In contrast, the absolute value of ΔG(H) for OD-$La_{0.40}$-CuO_x, at 0.14 eV, is substantially lower than that of OD-CuO_x without La doping and OD-$La_{0.10}$-CuO_x (0.74 eV and 0.82 eV, respectively) (Fig. 6**f**). This reveals the high activity of OD-$La_{0.40}$-CuO_x for HER, aligning with electrochemical test results (Fig. S21).

Therefore, based on insights from *in situ* spectroscopy and theoretical analyses, it can be concluded that OD-$La_{0.10}$-CuO_x and OD-$La_{0.40}$-CuO_x exhibit distinctive capacities for water dissociation, resulting in varied *H availability on their respective surfaces. As illustrated in Fig. 6**g**, the presence of moderate *H on the OD-$La_{0.10}$-CuO_x surface and abundant *H on the OD-$La_{0.40}$-CuO_x surface lead to different *CHO conversion pathways, lowering energy barriers for both dimerization (*CHO → *OCCHO) and hydrogenation (*CHO → *CH_2O) processes, thereby achieving enhanced CO_2RR performance towards C_{2+} products and CH_4. These differences can be attributed to the varied dependence on proton transfer in the RDS for CO_2RR-to-C_{2+}/CH_4. According to KIE results, the CO_2RR-to-C_{2+} process may lack a distinct proton-related RDS or involve multiple parallel proton-related RDSs, whereas the CO_2RR-to-CH_4 process is significantly influenced by proton transfer in its RDS. These findings are in line with observations from electrochemical performance tests and kinetic studies.

4. Conclusions

In summary, we have developed a series of OD-La-CuO_x catalysts with tailored adsorbed hydrogen (*H) to achieve controlled industrial-current-density CO_2 conversion to C_{2+} products and CH_4. The OD-$La_{0.10}$-CuO_x catalyst exhibits outstanding performance of CO_2RR to C_{2+} products in 1 M KCl, reaching a Faradaic efficiency (FE) of 80.4% for C_{2+} products at a current density of 300 mA cm^{-2}. Conversely, with increased La doping in OD-$La_{0.40}$-CuO_x, a maximum FE of 61.5% for CH_4 is achieved at 400 mA cm^{-2} in 1 M KOH. Both experimental and kinetic studies reveal that increased La doping alters the phase composition of OD-La-CuO_x catalysts and correlates positively with higher concentrations of *H, allowing for tunable electron selectivity and kinetics of CO_2RR products. Notably, *in situ* ATR-SEIRAS and DFT studies demonstrate that the OD-La-CuO_x catalysts possess varying H_2O dissociation capacities, accounting for their variations in *H. Additionally, this modulation strategy can guide the reaction pathway toward either *CHO dimerization or hydrogenation, thereby lowering reaction barriers for producing target C_{2+} products and CH_4. OD-$La_{0.10}$-CuO_x, with its moderate H_2O dissociation capacity, favors the *CO → *CHO and *CHO → *OCCHO pathways, enhancing C-C coupling and leading to C_{2+} production. In contrast, OD-$La_{0.40}$-CuO_x, characterized by the lowest H_2O dissociation energy barrier, enhances proton transfer, promoting CO_2RR-to-CH_4 via the *CHO → *CH_2O pathway. The findings from this study provide a promising strategy for optimizing the selectivity of target CO_2RR products at industrial current densities.

CRediT authorship contribution statement

Zeyu Guo: Conceptualization, Methodology, Investigation, Formal analysis, Writing – original draft. **Huiwen Zhu**: Data curation, Validation, Methodology. **Zijun Yan**: Formal analysis, Data curation. **Lei Lei:** Methodology, Formal analysis. **Degao Wang:** Resources, Writing – review & editing. **Ziyun Xi**: Investigation, Data curation. **Yirui Lian:** Formal analysis, Data curation. **Jiahui Yu:** Data curation, Methodology, Funding acquisition. **Kam Loon Fow:** Supervision, Writing – review & editing. **Hainam Do:** Supervision, Writing – review & editing. **Jonathan**

D. Hirst: Supervision, Writing – review & editing. **Tao Wu:** Supervision, Resources, Writing – review & editing. **Mengxia Xu:** Funding acquisition, Supervision, Writing – review & editing.

Declaration of Competing Interest

The authors declare that they have no known competing financial interests or personal relationships that could have appeared to influence the work reported in this paper.

Acknowledgments

This work is financially supported by Ningbo Science and Technology Bureau (2021S097), and the Department of Science and Technology of Zhejiang Province (LGF22B060009). J.Y expresses gratitude for the financial support from the National Natural Science Foundation of China (22308195) and the Natural Science Foundation of Shandong Province (ZR2023QB237). J.D.H receives support from the Royal Academy of Engineering under the Chairs in Emerging Technologies scheme (CiET2021_17). Z.G. acknowledges the full Ph.D. scholarship provided by University of Nottingham Ningbo China.

Declaration of competing interest

The authors declare no competing financial interest.

Appendix. Supporting Information

Supplementary data associated with this article can be found in the attached file.

Appendix A. Supporting information

Supplementary data associated with this article can be found in the online version at doi:10.1016/j.apcatb.2024.124839.

Data Availability

Data will be made available on request. No data was used for the research described in the article.

References

[1] F.P. García de Arquer, C.-T. Dinh, A. Ozden, J. Wicks, C. McCallum, A.R. Kirmani, D.-H. Nam, C. Gabardo, A. Seifitokaldani, X. Wang, Y.C. Li, F. Li, J. Edwards, L. J. Richter, S.J. Thorpe, D. Sinton, E.H. Sargent, CO_2 electrolysis to multicarbon products at activities greater than 1 A cm^{-2}, Science 367 (2020) 661–666.

[2] Z. Guo, F. Yang, X. Li, H. Zhu, H. Do, K. Loon Fow, J.D. Hirst, T. Wu, Q. Ye, Y. Peng, H. Bin Wu, A. Wu, M. Xu, Electrocatalytic CO_2 reduction to C_2H_4: From lab to fab, J. Energy Chem. 90 (2024) 540–564.

[3] D. Wakerley, S. Lamaison, J. Wicks, A. Clemens, J. Feaster, D. Corral, S.A. Jaffer, A. Sarkar, M. Fontecave, E.B. Duoss, S. Baker, E.H. Sargent, T.F. Jaramillo, C. Hahn, Gas diffusion electrodes, reactor designs and key metrics of low-temperature CO_2 electrolysers, Nat. Energy 7 (2022) 130–143.

[4] D.-H. Nam, O. Shekhah, A. Ozden, C. McCallum, F. Li, X. Wang, Y. Lum, T. Lee, J. Li, J. Wicks, A. Johnston, D. Sinton, M. Eddaoudi, E.H. Sargent, High-rate and selective CO_2 electrolysis to ethylene via metal–organic-framework-augmented CO_2 availability, Adv. Mater. 34 (2022) 2207088.

[5] R.I. Masel, Z. Liu, H. Yang, J.J. Kaczur, D. Carrillo, S. Ren, D. Salvatore, C. P. Berlinguette, An industrial perspective on catalysts for low-temperature CO_2 electrolysis, Nat. Nanotechnol. 16 (2021) 118–128.

[6] G.M. Tomboc, S. Choi, T. Kwon, Y.J. Hwang, K. Lee, Potential link between Cu surface and selective CO_2 electroreduction: perspective on future electrocatalyst designs, Adv. Mater. 32 (2020) 1908398.

[7] J. Zhao, P. Zhang, T. Yuan, D. Cheng, S. Zhen, H. Gao, T. Wang, Z.-J. Zhao, J. Gong, Modulation of $*CH_xO$ adsorption to facilitate electrocatalytic reduction of CO_2 to CH_4 over Cu-based catalysts, J. Am. Chem. Soc. 145 (2023) 6622–6627.

[8] Z. Xu, C. Peng, G. Luo, S. Yang, P. Yu, S. Yan, M. Shakouri, Z. Wang, T.-K. Sham, G. Zheng, High-rate CO_2-to-CH_4 electrosynthesis by undercoordinated Cu Sites in alkaline-earth-metal perovskites with strong basicity, Adv. Energy Mater. 13 (2023) 2204417.

[9] X. Chen, S. Jia, C. Chen, J. Jiao, J. Zhai, T. Deng, C. Xue, H. Cheng, M. Dong, W. Xia, J. Zeng, X. Xing, H. Wu, M. He, B. Han, Highly stable layered coordination polymer electrocatalyst toward efficient CO_2-to-CH_4 conversion, Adv. Mater., N./a (2023) 2310273.

[10] X. Chen, J. Chen, N.M. Alghoraibi, D.A. Henckel, R. Zhang, U.O. Nwabara, K. E. Madsen, P.J.A. Kenis, S.C. Zimmerman, A.A. Gewirth, Electrochemical CO_2-to-ethylene conversion on polyamine-incorporated Cu electrodes, Nat. Catal. 4 (2021) 20–27.

[11] W. Ma, S. Xie, T. Liu, Q. Fan, J. Ye, F. Sun, Z. Jiang, Q. Zhang, J. Cheng, Y. Wang, Electrocatalytic reduction of CO_2 to ethylene and ethanol through hydrogen-assisted C–C coupling over fluorine-modified copper, Nat. Catal. 3 (2020) 478–487.

[12] F. Li, A. Thevenon, A. Rosas-Hernández, Z. Wang, Y. Li, C.M. Gabardo, A. Ozden, C. T. Dinh, J. Li, Y. Wang, J.P. Edwards, Y. Xu, C. McCallum, L. Tao, Z.-Q. Liang, M. Luo, X. Wang, H. Li, C.P. O'Brien, C.-S. Tan, D.-H. Nam, R. Quintero-Bermudez, T.-T. Zhuang, Y.C. Li, Z. Han, R.D. Britt, D. Sinton, T. Agapie, J.C. Peters, E. H. Sargent, Molecular tuning of CO_2-to-ethylene conversion, Nature 577 (2020) 509–513.

[13] C.-T. Dinh, T. Burdyny, M.G. Kibria, A. Seifitokaldani, C.M. Gabardo, F.P. García de Arquer, A. Kiani, J.P. Edwards, P. De Luna, O.S. Bushuyev, C. Zou, R. Quintero-Bermudez, Y. Pang, D. Sinton, E.H. Sargent, CO_2 electroreduction to ethylene via hydroxide-mediated copper catalysis at an abrupt interface, Science 360 (2018) 783–787.

[14] M. Wang, H. Chen, M. Wang, J. Wang, Y. Tuo, W. Li, S. Zhou, L. Kong, G. Liu, L. Jiang, G. Wang, Tuning C1/C2 selectivity of CO_2 electrochemical reduction over in-situ evolved CuO/SnO_2 heterostructure, Angew. Chem. Int. Ed. 62 (2023) e202306456.

[15] Y. Cui, C. Kong, C. Yang, Y. Su, Y. Cheng, D. Yao, G. Chen, K. Song, Z. Zhong, Y. Song, G. Wang, Z. Li, L. Zhuang, N_xC-induced switching of methane and ethylene products' selectivity from CO_2 electroreduction over Cu catalyst, ACS Catal. 13 (2023) 11625–11633.

[16] S. Liu, H.B. Yang, S.-F. Hung, J. Ding, W. Cai, L. Liu, J. Gao, X. Li, X. Ren, Z. Kuang, Y. Huang, T. Zhang, B. Liu, Elucidating the electrocatalytic CO_2 reduction reaction over a model single-atom nickel catalyst, Angew. Chem. Int. Ed. 59 (2020) 798–803.

[17] L. Xiong, X. Zhang, L. Chen, Z. Deng, S. Han, Y. Chen, J. Zhong, H. Sun, Y. Lian, B. Yang, X. Yuan, H. Yu, Y. Liu, X. Yang, J. Guo, M.H. Rümmeli, Y. Jiao, Y. Peng, Geometric modulation of local CO flux in Ag@Cu_2O nanoreactors for steering the CO_2RR pathway toward high-efficacy methane production, Adv. Mater. 33 (2021) 2101741.

[18] Y. Kim, S. Park, S.-J. Shin, W. Choi, B.K. Min, H. Kim, W. Kim, Y.J. Hwang, Time-resolved observation of C–C coupling intermediates on Cu electrodes for selective electrochemical CO_2 reduction, Energ. Environ. Sci. 13 (2020) 4301–4311.

[19] A.J. Garza, A.T. Bell, M. Head-Gordon, Mechanism of CO_2 reduction at copper surfaces: pathways to C_2 products, ACS Catal. 8 (2018) 1490–1499.

[20] J. Santatiwongchai, K. Faungnawakij, P. Hirunsit, Comprehensive mechanism of CO_2 electroreduction toward ethylene and ethanol: the solvent effect from explicit water–Cu(100) interface models, ACS Catal. 11 (2021) 9688–9701.

[21] B.A. Zhang, C. Costentin, D.G. Nocera, On the conversion efficiency of CO_2 electroreduction on gold, Joule 3 (2019) 1565–1568.

[22] Y. Lum, T. Cheng, W.A. Goddard III, J.W. Ager, Electrochemical CO reduction builds solvent water into oxygenate products, J. Am. Chem. Soc. 140 (2018) 9337–9340.

[23] X. Chen, J. Chen, H. Chen, Q. Zhang, J. Li, J. Cui, Y. Sun, D. Wang, J. Ye, L. Liu, Promoting water dissociation for efficient solar driven CO_2 electroreduction via improving hydroxyl adsorption, Nat. Commun. 14 (2023) 751.

[24] D. Misra, G. Di Liberto, G. Pacchioni, CO_2 electroreduction on single atom catalysts: is water just a solvent? J. Catal. 422 (2023) 1–11.

[25] Z. Guo, H. Zhu, G. Yang, A. Wu, Q. Chen, Z. Yan, K. Loon Fow, H. Do, J.D. Hirst, T. Wu, M. Xu, Synergistic engineering of heteronuclear Ni-Ag dual-atom catalysts for high-efficiency CO_2 electroreduction with nearly 100% CO selectivity, Chem. Eng. J. 476 (2023) 146556.

[26] H. Wang, X. Kang, B. Han, Rare-earth element-based electrocatalysts designed for CO_2 electro-reduction, ChemSusChem 17 (2024) e202301539.

[27] J. Feng, L. Zhang, S. Liu, L. Xu, X. Ma, X. Tan, L. Wu, Q. Qian, T. Wu, J. Zhang, X. Sun, B. Han, Modulating adsorbed hydrogen drives electrochemical CO_2-to-C_2 products, Nat. Commun. 14 (2023) 4615.

[28] S. You, J. Xiao, S. Liang, W. Xie, T. Zhang, M. Li, Z. Zhong, Q. Wang, H. He, Doping engineering of Cu-based catalysts for electrocatalytic CO_2 reduction to multi-carbon products, Energ. Environ. Sci. 17 (2024) 5795–5818.

[29] S. Hu, Y. Chen, Z. Zhang, S. Li, H. Liu, X. Kang, J. Liu, S. Ge, J. Wang, W. Lv, Z. Zeng, X. Zou, Q. Yu, B. Liu, Ampere-level current density CO_2 reduction with high C_{2+} selectivity on La$(OH)_3$-modified Cu catalysts, Small 20 (2024) 2308226.

[30] J. Wang, C. Cheng, B. Huang, J. Cao, L. Li, Q. Shao, L. Zhang, X. Huang, Grain-boundary-engineered La_2CuO_4 perovskite nanobamboos for efficient CO_2 reduction reaction, Nano Lett. 21 (2021) 980–987.

[31] Y. Xie, P. Ou, X. Wang, Z. Xu, Y.C. Li, Z. Wang, J.E. Huang, J. Wicks, C. McCallum, N. Wang, Y. Wang, T. Chen, B.T.W. Lo, D. Sinton, J.C. Yu, Y. Wang, E.H. Sargent, High carbon utilization in CO_2 reduction to multi-carbon products in acidic media, Nat. Catal. 5 (2022) 564–570.

[32] W. Li, Z. Yin, Z. Gao, G. Wang, Z. Li, F. Wei, X. Wei, H. Peng, X. Hu, L. Xiao, J. Lu, L. Zhuang, Bifunctional ionomers for efficient co-electrolysis of CO_2 and pure water towards ethylene production at industrial-scale current densities, Nat. Energy 7 (2022) 835–843.

[33] Z.-s Hong, Y. Cao, J.-f Deng, A convenient alcohothermal approach for low temperature synthesis of CuO nanoparticles, Mater. Lett. 52 (2002) 34–38.

[34] Y. Wang, Z. Chen, P. Han, Y. Du, Z. Gu, X. Xu, G. Zheng, Single-atomic Cu with multiple oxygen vacancies on ceria for electrocatalytic CO_2 reduction to CH_4, ACS Catal. 8 (2018) 7113–7119.

[35] X. Zhong, S. Liang, T. Yang, G. Zeng, Z. Zhong, H. Deng, L. Zhang, X. Sun, Sn dopants with synergistic oxygen vacancies boost CO_2 electroreduction on CuO nanosheets to CO at low overpotential, ACS Nano 16 (2022) 19210–19219.

[36] X. Wang, L. Shi, W. Ren, J. Li, Y. Liu, W. Fu, S. Wang, S. Yao, Y. Ji, K. Ji, L. Zhang, Z. Yang, J. Xie, Y.-M. Yan, Enhancing *CO coverage on Sm-Cu_2O via 4f-3d orbital hybridization for highly efficient electrochemical CO_2 reduction to C_2H_4, J. Energy Chem. 99 (2024) 409–416.

[37] Y. Sun, J. Xie, Z. Fu, H. Zhang, Y. Yao, Y. Zhou, X. Wang, S. Wang, X. Gao, Z. Tang, S. Li, X. Wang, K. Nie, Z. Yang, Y.-M. Yan, Boosting CO_2 electroreduction to C_2H_4 via unconventional hybridization: high-Order Ce^{4+} 4f and O 2p interaction in Ce-Cu_2O for stabilizing Cu^+, ACS Nano 17 (2023) 13974–13984.

[38] Y. Zhou, Y. Yao, R. Zhao, X. Wang, Z. Fu, D. Wang, H. Wang, L. Zhao, W. Ni, Z. Yang, Y.-M. Yan, Stabilization of Cu^+ via strong electronic interaction for selective and stable CO_2 electroreduction, Angew. Chem. Int. Ed. 61 (2022) e202205832.

[39] Y. Sun, X. Wang, H. Zhang, X. Gao, X. Wang, S. Wang, Z. Tang, S. Li, K. Nie, J. Xie, Z. Yang, Y.-M. Yan, Deciphering the stability mechanism of Cu active sites in CO_2 electroreduction via suppression of antibonding orbital occupancy in the O 2p-Cu 3d hybridization, ACS Catal. 14 (2024) 1351–1362.

[40] H. Zhang, X. Wang, Y. Sun, X. Wang, Z. Tang, S. Li, X. Gao, J. Wang, Z. Hou, K. Nie, J. Xie, Z. Yang, Y.-M. Yan, Targeted C-O bond cleavage of $*CH_2CHO$ at copper active sites for efficient electrosynthesis of ethylene from CO_2 reduction, Appl. Catal., B 351 (2024) 123992.

[41] M. Uma, N. Balaram, P.R. Sekhar Reddy, V. Janardhanam, V.Rajagopal Reddy, H.-J. Yun, S.-N. Lee, C.-J. Choi, Structural, chemical and electrical properties of Au/La_2O_3/n-GaN MIS junction with a high-k lanthanum oxide insulating layer, J. Electron. Mater. 48 (2019) 4217–4225.

[42] Z. Gu, N. Yang, P. Han, M. Kuang, B. Mei, Z. Jiang, J. Zhong, L. Li, G. Zheng, Oxygen vacancy tuning toward efficient electrocatalytic CO_2 reduction to C_2H_4, Small Methods 3 (2019) 1800449.

[43] S. Chen, Y. Su, P. Deng, R. Qi, J. Zhu, J. Chen, Z. Wang, L. Zhou, X. Guo, B.Y. Xia, Highly selective carbon dioxide electroreduction on structure-evolved copper perovskite oxide toward methane production, ACS Catal. 10 (2020) 4640–4646.

[44] K. Chu, F. Liu, J. Zhu, H. Fu, H. Zhu, Y. Zhu, Y. Zhang, F. Lai, T. Liu, A general strategy to boost electrocatalytic nitrogen reduction on perovskite oxides via the oxygen vacancies derived from a-site deficiency, Adv. Energy Mater. 11 (2021) 2003799.

[45] J. Zhu, Y. Wang, A. Zhi, Z. Chen, L. Shi, Z. Zhang, Y. Zhang, Y. Zhu, X. Qiu, X. Tian, X. Bai, Y. Zhang, Y. Zhu, Cation-deficiency-dependent CO_2 electroreduction over copper-based ruddlesden–popper perovskite oxides, Angew. Chem. Int. Ed. 61 (2022) e202111670.

[46] X. Chang, M. He, Q. Lu, B. Xu, Origin and effect of surface oxygen-containing species on electrochemical CO or CO_2 reduction reactions, Sci. China Chem. 66 (2023) 96–106.

[47] Y.-R. Wang, M. Liu, G.-K. Gao, Y.-L. Yang, R.-X. Yang, H.-M. Ding, Y. Chen, S.-L. Li, Y.-Q. Lan, Implanting numerous hydrogen-bonding networks in a Cu-porphyrin-based nanosheet to boost CH_4 selectivity in neutral-media CO_2 electroreduction, Angew. Chem. Int. Ed. 60 (2021) 21952–21958.

[48] X. Zhang, J. Li, Y.-Y. Li, Y. Jung, Y. Kuang, G. Zhu, Y. Liang, H. Dai, Selective and high current CO_2 electro-reduction to multicarbon products in near-neutral KCl electrolytes, J. Am. Chem. Soc. 143 (2021) 3245–3255.

[49] Y. Wang, J. Zhang, J. Zhao, Y. Wei, S. Chen, H. Zhao, Y. Su, S. Ding, C. Xiao, Strong hydrogen-bonded interfacial water inhibiting hydrogen evolution kinetics to promote electrochemical CO_2 reduction to C_{2+}, ACS Catal. 14 (2024) 3457–3465.

[50] Y. Li, F. Liu, Z. Chen, L. Shi, Z. Zhang, Y. Gong, Y. Zhang, X. Tian, Y. Zhang, X. Qiu, X. Ding, X. Bai, H. Jiang, Y. Zhu, J. Zhu, Perovskite-socketed sub-3 nm copper for enhanced CO_2 electroreduction to C_{2+}, Adv. Mater. 34 (2022) 2206002.

[51] J. Sang, P. Wei, T. Liu, H. Lv, X. Ni, D. Gao, J. Zhang, H. Li, Y. Zang, F. Yang, Z. Liu, G. Wang, X. Bao, A reconstructed $Cu_2P_2O_7$ catalyst for selective CO_2 electroreduction to multicarbon products, Angew. Chem. Int. Ed. 61 (2022) e202114238.

[52] Y. Song, J.R.C. Junqueira, N. Sikdar, D. Öhl, S. Dieckhöfer, T. Quast, S. Seisel, J. Masa, C. Andronescu, W. Schuhmann, B-Cu-Zn gas diffusion electrodes for CO_2 electroreduction to C_{2+} products at high current densities, Angew. Chem. Int. Ed. 60 (2021) 9135–9141.

[53] R. Wang, J. Liu, Q. Huang, L.-Z. Dong, S.-L. Li, Y.-Q. Lan, Partial coordination-perturbed Bi-copper sites for selective electroreduction of CO_2 to hydrocarbons, Angew. Chem. Int. Ed. 60 (2021) 19829–19835.

[54] C. Chen, Y. Li, S. Yu, S. Louisia, J. Jin, M. Li, M.B. Ross, P. Yang, Cu-Ag tandem catalysts for high-rate CO_2 electrolysis toward multicarbons, Joule 4 (2020) 1688–1699.

[55] Z.-Z. Niu, F.-Y. Gao, X.-L. Zhang, P.-P. Yang, R. Liu, L.-P. Chi, Z.-Z. Wu, S. Qin, X. Yu, M.-R. Gao, Hierarchical copper with inherent hydrophobicity mitigates electrode flooding for high-rate CO_2 electroreduction to multicarbon products, J. Am. Chem. Soc. 143 (2021) 8011–8021.

[56] Z.-Z. Wu, X.-L. Zhang, Z.-Z. Niu, F.-Y. Gao, P.-P. Yang, L.-P. Chi, L. Shi, W.-S. Wei, R. Liu, Z. Chen, S. Hu, X. Zheng, M.-R. Gao, Identification of Cu(100)/Cu(111) interfaces as superior active sites for CO dimerization during CO_2 electroreduction, J. Am. Chem. Soc. 144 (2022) 259–269.

[57] K. Yao, J. Li, H. Wang, R. Lu, X. Yang, M. Luo, N. Wang, Z. Wang, C. Liu, T. Jing, S. Chen, E. Cortés, S.A. Maier, S. Zhang, T. Li, Y. Yu, Y. Liu, X. Kang, H. Liang, Mechanistic insights into OC–COH coupling in CO_2 electroreduction on fragmented copper, J. Am. Chem. Soc. 144 (2022) 14005–14011.

[58] S. Wang, J. Zhang, L. Yao, Y. Yang, L. Zheng, B. Guan, Y. Zhao, Y. Wang, B. Han, X. Xing, Efficient electrocatalytic CO_2 reduction to C_{2+} chemicals on internal porous copper, Nano Res. 16 (2023) 10779–10786.

[59] B. Yang, K. Liu, H. Li, C. Liu, J. Fu, H. Li, J.E. Huang, P. Ou, T. Alkayyali, C. Cai, Y. Duan, H. Liu, P. An, N. Zhang, W. Li, X. Qiu, C. Jia, J. Hu, L. Chai, Z. Lin, Y. Gao, M. Miyauchi, E. Cortés, S.A. Maier, M. Liu, Accelerating CO_2 electroreduction to multicarbon products via synergistic electric–thermal field on copper nanoneedles, J. Am. Chem. Soc. 144 (2022) 3039–3049.

[60] G. Zhang, Z.-J. Zhao, D. Cheng, H. Li, J. Yu, Q. Wang, H. Gao, J. Guo, H. Wang, G. A. Ozin, T. Wang, J. Gong, Efficient CO_2 electroreduction on facet-selective copper films with high conversion rate, Nat. Commun. 12 (2021) 5745.

[61] M. He, X. Chang, T.-H. Chao, C. Li, W.A. Goddard III, M.-J. Cheng, B. Xu, Q. Lu, Selective enhancement of methane formation in electrochemical CO_2 reduction enabled by a Raman-inactive oxygen-containing species on Cu, ACS Catal. 12 (2022) 6036–6046.

[62] G. Wen, B. Ren, M.G. Park, J. Yang, H. Dou, Z. Zhang, Y.-P. Deng, Z. Bai, L. Yang, J. Gostick, G.A. Botton, Y. Hu, Z. Chen, Ternary Sn-Ti-O electrocatalyst boosts the stability and energy efficiency of CO_2 reduction, Angew. Chem. Int. Ed. 59 (2020) 12860–12867.

[63] Y. Zhang, F. Chen, X. Hao, Y. Liu, W. Wu, X. Zhang, Z. Zang, H. Dong, W. Wang, F. Lu, Z. Lu, H. Liu, H. Liu, F. Luo, Y. Cheng, Enhanced interfacial effect-induced asymmetric coupling boost electroreduction of CO_2 to ethylene, Appl. Catal., B 344 (2024) 123666.

[64] X. Wang, A. Xu, F. Li, S.-F. Hung, D.-H. Nam, C.M. Gabardo, Z. Wang, Y. Xu, A. Ozden, A.S. Rasouli, A.H. Ip, D. Sinton, E.H. Sargent, Efficient methane electrosynthesis enabled by tuning local CO_2 availability, J. Am. Chem. Soc. 142 (2020) 3525–3531.

[65] S. Bai, L. Tan, C. Ning, G. Liu, Z. Wu, T. Shen, L. Zheng, Y.-F. Song, Revealing the kinetic balance between proton-feeding and hydrogenation in CO_2 electroreduction, Small 19 (2023) 2300581.

[66] J. Lv, A. Wu, L. Wang, Y. Zhong, Z. Zeng, Q. Huang, X. Lin, H. Zhang, S. Liu, Q. Liu, S. Zhu, X. Li, J. Yan, Z. Qi, H.Bin Wu, Zeolite-mediated hybrid Cu^{+}/Cu^{0} interface for electrochemical nitrate reduction to ammonia, J. Energy Chem. 87 (2023) 136–143.

[67] J. Yin, J. Jin, Z. Yin, L. Zhu, X. Du, Y. Peng, P. Xi, C.-H. Yan, S. Sun, The built-in electric field across FeN/Fe_3N interface for efficient electrochemical reduction of CO_2 to CO, Nat. Commun. 14 (2023) 1724.

[68] J. Li, J. Li, X. Liu, J. Chen, P. Tian, S. Dai, M. Zhu, Y.-F. Han, Probing the role of surface hydroxyls for Bi, Sn and In catalysts during CO_2 Reduction, Appl. Catal., B 298 (2021) 120581.

[69] D.B. Northrop, Steady-state analysis of kinetic isotope effects in enzymic reactions, Biochemistry 14 (1975) 2644–2651.

[70] Y. Liu, C.C.L. McCrory, Modulating the mechanism of electrocatalytic CO_2 reduction by cobalt phthalocyanine through polymer coordination and encapsulation, Nat. Commun. 10 (2019) 1683.

[71] N.V. Krstajić, B.N. Grgur, N.S. Mladenović, M.V. Vojnović, M.M. Jakšić, The determination of kinetics parameters of the hydrogen evolution on Ti Ni alloys by ac impedance, Electrochim. Acta 42 (1997) 323–330.

[72] T. Zhang, B. Yuan, W. Wang, J. He, X. Xiang, Tailoring *H intermediate coverage on the $CuAl_2O_4$/CuO catalyst for enhanced electrocatalytic CO_2 reduction to ethanol, Angew. Chem. Int. Ed. 62 (2023) e202302096.

[73] N. Meng, C. Liu, Y. Liu, Y. Yu, B. Zhang, Efficient electrosynthesis of syngas with tunable CO/H_2 ratios over $Zn_xCd_{1-x}S$-amine inorganic–organic hybrids, Angew. Chem. Int. Ed. 58 (2019) 18908–18912.

[74] Z. Lv, C. Wang, Y. Liu, R. Liu, F. Zhang, X. Feng, W. Yang, B. Wang, Improving CO_2-to-C_2 conversion of atomic CuFONC electrocatalysts through F, O-codrived optimization of local coordination environment, Adv. Energy Mater. 14 (2024) 2400057.

[75] E.P. Delmo, Y. Wang, Y. Song, S. Zhu, H. Zhang, H. Xu, T. Li, J. Jang, Y. Kwon, Y. Wang, M. Shao, In Situ infrared spectroscopic evidence of enhanced electrochemical CO_2 reduction and C–C coupling on oxide-derived copper, J. Am. Chem. Soc. 146 (2024) 1935–1945.

[76] Y. Yu, Y. He, P. Yan, S. Wang, F. Dong, Boosted C–C coupling with Cu–Ag alloy sub-nanoclusters for CO_2-to-C_2H_4 photosynthesis, Proc. Natl. Acad. Sci. 120 (2023) e2307320120.

[77] X.-F. Qiu, J.-R. Huang, C. Yu, Z.-H. Zhao, H.-L. Zhu, Z. Ke, P.-Q. Liao, X.-M. Chen, A stable and conductive covalent organic framework with isolated active sites for highly selective electroreduction of carbon dioxide to acetate, Angew. Chem. Int. Ed. 61 (2022) e202206470.

[78] J.-D. Yi, R. Xie, Z.-L. Xie, G.-L. Chai, T.-F. Liu, R.-P. Chen, Y.-B. Huang, R. Cao, Highly selective CO_2 electroreduction to CH_4 by insitu generated Cu_2O single-type sites on a conductive MOF: stabilizing key intermediates with hydrogen bonding, Angew. Chem. Int. Ed. 59 (2020) 23641–23648.

[79] J. Cheng, L. Chen, X. Xie, K. Feng, H. Sun, Y. Qin, W. Hua, Z. Zheng, Y. He, W. Pan, W. Yang, F. Lyu, J. Zhong, Z. Deng, Y. Jiao, Y. Peng, Proton shuttling by polyaniline of high Brønsted basicity for improved electrocatalytic ethylene production from CO_2, Angew. Chem. Int. Ed. 62 (2023) e202312113.

[80] Q. Fan, X. Zhang, X. Ge, L. Bai, D. He, Y. Qu, C. Kong, J. Bi, D. Ding, Y. Cao, X. Duan, J. Wang, J. Yang, Y. Wu, Manipulating Cu nanoparticle surface oxidation states tunes catalytic selectivity toward CH_4 or C_{2+} products in CO_2 electroreduction, Adv. Energy Mater. 11 (2021) 2101424.

[81] Y. Liang, J. Zhao, Y. Yang, S.-F. Hung, J. Li, S. Zhang, Y. Zhao, A. Zhang, C. Wang, D. Appadoo, L. Zhang, Z. Geng, F. Li, J. Zeng, Stabilizing copper sites in coordination polymers toward efficient electrochemical C-C coupling, Nat. Commun. 14 (2023) 474.